EDITORS' CHOICE / INVITED REVIEW

A Review of the Extended EUV Corona Observed by the *Sun Watcher with Active Pixels and Image Processing* (SWAP) Instrument

Matthew J. West[1] · Daniel B. Seaton[1] · Elke D'Huys[2] · Marilena Mierla[2,3] ·
Monica Laurenza[4] · Karen A. Meyer[5] · David Berghmans[2] ·
Laurel R. Rachmeler[6] · Luciano Rodriguez[2] · Koen Stegen[2]

Abstract

The *Sun Watcher with Active Pixels and Image Processing* (SWAP) instrument on-board ESA's *PRoject for On Board Autonomy 2* (PROBA2) has provided the first un-compressed, high-cadence, continuous, large field-of-view observations of the extended extreme-ultraviolet (EUV) corona for over a complete solar cycle. It has helped shape our understanding of this previously understudied region, and pioneered research into the middle corona. In this article, we present a review of all publications that have utilized these observations to explore the extended EUV corona, highlighting the unique contributions made by SWAP. The review is broadly divided into three main sections of SWAP-based studies about: i) long-lived phenomena, such as streamers, pseudo-streamers, and coronal fans; ii) dynamic phenomena, such as eruptions, jets, EUV waves, and shocks; iii) coronal EUV emission generation. We also highlight SWAP's imaging capabilities, techniques that have been applied to observations to enhance the off-limb observations and its legacy.

Keywords Coronal mass ejections, low coronal signatures · Coronal mass ejections, initiation and propagation · Corona, structures · Instrumentation and data management · Jets · Prominences, formation and evolution · Radio bursts

✉ M.J. West
   mwest@boulder.swri.edu

1   Southwest Research Institute, 1050 Walnut Street, Suite 300, Boulder, CO 80302, USA

2   Solar-Terrestrial Centre of Excellence – SIDC, Royal Observatory of Belgium, Avenue Circulaire 3, 1180 Brussels, Belgium

3   Institute of Geodynamics of the Romanian Academy, Bucharest, Romania

4   Institute of Space Astrophysics and Planetology - INAF, Via del Fosso del Cavaliere, 00133 Roma, Italy

5   Mathematics, School of Science & Engineering, University of Dundee, Nethergate, Dundee DD1 4HN, UK

6   NOAA National Centers for Environmental Information, 325 Broadway, Boulder, CO 80305, USA

1. Introduction

The *Sun Watcher with Active Pixels and Image Processing* instrument (SWAP: Seaton et al., 2013b; Halain et al., 2013) is a large field-of-view (FOV) extreme-ultraviolet (EUV) observing telescope onboard the European Space Agency's (ESA) *Project for Onboard Autonomy 2* (PROBA2) spacecraft (Santandrea et al., 2013), observing a FOV of $\approx 1.7 \times 1.7$ solar radii (as measured from the disk center; $R_\odot$ hereon), or 54×54 arcmin, along the image axes, and 2.5 $R_\odot$ along the diagonal. This is spread over 1024×1024 pixels, with 3.17 arcsec pixel^{-1}. SWAP produces some of the largest FOV images of the off-limb EUV corona, which we will describe as the extended EUV corona. SWAP was designed to monitor all space-weather-related phenomena through a spectral bandpass centered on 17.4 nm, around the Fe IX/X emission lines, corresponding to an observing temperature of $T \approx 0.8$ MK.

PROBA2, launched in November 2009, was originally designed as a technology-demonstration mission with a secondary mission goal to exploit the payload of the scientific instruments, including the SWAP EUV instrument. The mission has been observing almost continuously since its launch, with a few gaps owing to calibration campaigns and its Sun-synchronous polar orbit, at an altitude of approximately 720 km, which creates short eclipse seasons for a few weeks per year (where the Earth occults SWAP's FOV). The short eclipse seasons only create sub-hour blind spots, which do not interfere with studies focused on long-term dynamics rather than transient studies.

As SWAP has been observing the Sun for over 12 years (at the time of writing), it allows us to capture the evolution of the corona over a whole solar cycle. This has provided the longest continuous set of observations of the extended EUV corona from the Earth's perspective. SWAP's nominal observation mode produces Sun-centered images, however, many PROBA2 off-point campaigns have been performed to extend the off-limb FOV in a particular direction.

SWAP observes dynamic events like flares, eruptions, EUV waves, and coronal dimmings. In addition, SWAP has continuously tracked long-lived structures such as streamers, coronal holes, and active regions, the locations of which are essential data for space-weather forecasting. SWAP's large FOV has also given researchers the ability to study the previously under-observed *middle corona.*

The middle corona is roughly defined as the region of the solar atmosphere extending from 1.5 to 6 $R_\odot$, and it has become synonymous with important transitions between the inner corona and the heliosphere. The middle corona is where the coronal fields transition from predominantly closed to open, and the plasma β (plasma gas pressure/magnetic pressure) transitions from low to high values. These transitions shape coronal structures, such as coronal mass ejections (CMEs: e.g. Webb and Howard, 2012; Zhang et al., 2021), jets (e.g. Sterling et al., 2015), supraarcade downflows (SADs: e.g. Savage, McKenzie, and Reeves, 2012; Shen et al., 2022) as well as the more static structures discussed above.

Prior to SWAP, the region known as the middle corona was largely overlooked from the Earth's perspective, and it was seldom studied using EUV imagery. Observing out from the inner corona, EUV and X-ray instrumentation required dedicated observing programs to capture the middle corona, sacrificing observations of the solar disk. SWAP's nominal observation program has allowed monitoring of background structures and transient structures alike. In addition, SWAP's deep-exposure data product (often referred to as Carrington data) combined multiple nominal observations to enhance off-limb sensitivity. These products are equivalent to long-exposure images, which blur transient phenomena but enhance longer-lived structures, such as coronal fans, streamers, and pseudo-streamers, which extend out into the heliosphere.

Observing inward from the heliosphere with white-light (WL) instruments is equally challenging; observations from compact WL space-based coronagraphs are significantly degraded close to the solar disk due to stray-light issues, and there are inherent difficulties associated with launching long-base-line instruments required to observe this region. Ground-based coronagraphs, meanwhile, can overcome some of these limitations, but must contend with background sky brightness and have a limited duty cycle. *The Large Angle and Spectrometric COronagraph* (LASCO: Brueckner et al., 1995) onboard the *SOlar and Heliospheric Observatory* (SOHO: Domingo, Fleck, and Poland, 1995) did incorporate the C1 coronagraph, which observed between 1.1 to 3 $R_\odot$ but was lost early in the mission.

The SWAP instrument has helped produce many publications that focus on the extended EUV corona, out into the middle corona, and phenomena that transition it. This article serves as a review of those articles. In Section 2 we provide an overview of the SWAP instrument and what it observes, and we compare it to other contemporary instruments; in Section 3 we present a review of observations that have utilized SWAP's large FOV for science, divided into dynamic and long-lived phenomena; in Section 4 we review articles that investigate coronal EUV-emission generation; in Section 5 we discuss the observations made by SWAP, and briefly discuss SWAP's legacy and the future of large field-of-view EUV imagery.

2. SWAP Observations

The SWAP design was largely driven by the limited spacecraft dimensions and the available mass budget combined with the program rationale to test new innovative technologies. Thus, SWAP was designed as a miniaturized off-axis two-mirror Ritchey–Chrétien coronal imager, with dimensions of $565 \times 150 \times 125$ mm, a mass of approximately 11 kg, and a peak power consumption of 2.6 W.

This design was largely facilitated by SWAP's combination of aluminum-foil filters and multi-layer coatings (Mo/Si) on the mirrors, achieving a bandpass centered on the 17.4-nm EUV wavelength, with 80% transmission, and allowing a small aperture size. This bandpass contains the brightest coronal emission lines in the EUV spectrum. The selected bandpass represents an excellent compromise between overall instrument sensitivity and sensitivity to the features associated with SWAP's science objectives.

In SWAP's camera, photons are collected on a CMOS (Complementary Metal-Oxide-Semiconductor) Active Pixel Sensor (APS) detector, covered by a phosphorous P43 scintillator coating, which absorbs EUV radiation and reemits it as visible light (at 545 nm) to which the CMOS-APS is sensitive (see Seaton et al., 2013b, for further details.) The CMOS-APS detector also facilitated a shutterless and non-blooming design.

Two representative SWAP images can be seen in Figure 1, taken near a solar maximum (left), and near a solar minimum (right). The images are composed of a stack of consecutive SWAP images (see Section 2.2). The stacked images enhance coherent signals over noise, allowing for the detection of faint structures in the extended EUV corona. These images show the changing activity of the Sun through the solar cycle, with increased numbers of active regions at the solar maximum, and large polar coronal holes at the solar minimum. They also show structures off the solar limb in the extended EUV atmosphere, including streamers, pseudo-streamers, and coronal-fan structures.

SWAP is one of several EUV instruments observing the Sun. A non-exhaustive list of contemporary instruments, with some key characteristics, includes: *Extreme ultraviolet Imaging Telescope* (EIT: Delaboudinière et al., 1995) onboard SOHO, which has been in operation since 1996, observing the Sun through four passbands, with peak wavelengths at
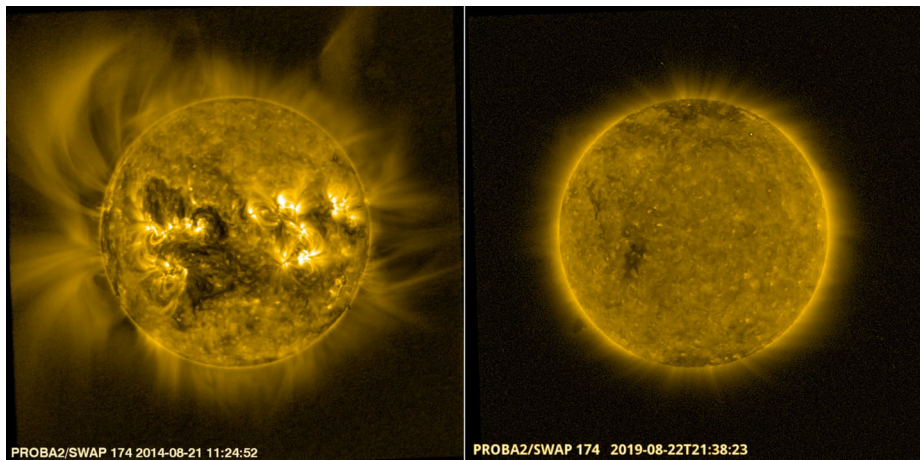
Figure 1 Two representative SWAP images, from 21 August 2014 near a solar maximum (*left*), and from 22 August 2019 near a solar minimum (*right*). The images are composed of stacked SWAP images (see Section 2.2) to increase signal-to-noise. The intensity scale is different in the two images.

17.1, 19.5, 28.4, and 30.4 nm; the twin *Extreme Ultraviolet Imagers* (EUVI: Wuelser et al., 2004) that are part of the *Sun Earth Connection Coronal and Heliospheric Investigation* (SECCHI: Howard et al., 2008) package onboard the *Solar TErrestrial RElations Observatory* (STEREO: Kaiser et al., 2008) spacecraft, launched in 2006, providing observations off the Sun–Earth line through passbands with peak wavelengths at 17.1, 19.5, 28.4, and 30.4 nm; and the *Atmospheric Imaging Assembly* (AIA: Lemen et al., 2012) onboard the *Solar Dynamics Observatory* (SDO: Pesnell, Thompson, and Chamberlin, 2012), which provides the highest resolution images of the solar disk along the Sun–Earth line (4096×4096 at 0.6 arcsec pixel^{-1}), passbands with peak wavelengths at 9.4, 13.1, 17.1, 19.3, 21.1, 30.4, and 33.5 nm. Since 2017 the *Solar Ultraviolet Imager* (SUVI: Darnel et al., 2022), on the several *Geostationary Operational Environmental Satellite* (GOES-R) spacecraft, has been observing through six passbands, with peak wavelengths at 9.4, 13.1, 17.1, 19.5, 28.4, and 30.4 nm, through a similar FOV to SWAP of $\approx 53'$. Since November 2021, the *Extreme Ultraviolet Imager* (EUI: Rochus et al., 2020) onboard *Solar Orbiter* (Müller et al., 2013) has been making observations of the solar atmosphere at various heliocentric distances, at times providing the highest resolution images of the solar disk, as well as some of the widest FOV images of the solar atmosphere. EUI will also provide the first-ever images of the Sun from an out-of-ecliptic viewpoint. EUI observes through bandpasses centered on 17.4 and 30.4 nm. Figure 2 shows a comparison of several contemporary EUV instruments, the relative FOVs, and passbands (peak temperatures) observed.

SWAP's response as a function of wavelength extends from 16.6 to 19.5 nm with a peak transmission near 17.4 nm and a secondary transmission peak at longer wavelengths. Although relatively narrow, it contains several lines including the Fe ɪх, Fe х, and Fe хɪ lines, formed across a range of temperatures and densities, which can originate from many heights in the corona. Raftery et al. (2013) calculated the sensitivity and temperature-response function of the SWAP passband, and compared it to that of EIT, the *Transition Region and Coronal Explorer* (TRACE: Handy et al., 1999), EUVI, and AIA. Raftery et al. found that although the wavelength responses for each instrument have some distinctly different features, the overall variation with temperature is consistent from instrument to instrument.
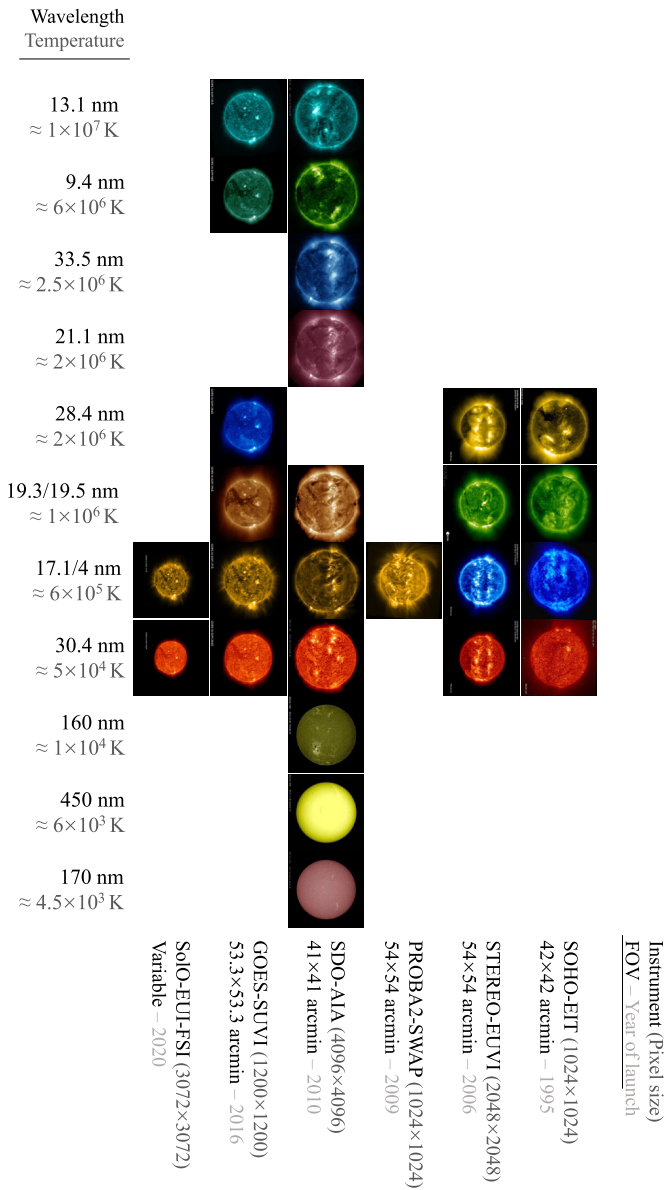
Figure 2 A comparison of available EUV imagers currently in operation. The rows are separated into pass-bands with the peak wavelength and characteristic temperature indicated. The columns indicate the instrument name and platform, pixel size, field-of-view (FOV), and year of launch. Note, images are rotated 90° clockwise, solar North is to the right.

Instruments such as EUVI and AIA offer a higher spatial resolution in comparison to SWAP, but the observing programs are designed to focus on solar-disk emission. EUVI has a comparable FOV to SWAP, but due to the heavy compression applied to the images, which is required in the telemetry-limited environment in which it operates, only the largest and

brightest structures can be monitored beyond a few megameters off of the solar limb. SWAP is the only instrument that has been monitoring the extended EUV solar atmosphere for over a complete solar cycle, and as a consequence has pioneered research in the middle corona.

2.1. Emission in the Extended Corona

As a result of the low-lying, hot, dense plasma, and the optically thin nature of the EUV observations, there is a large range in the intensity of emission (which can exceed 10^5) between the bright structures observed on-disk compared to those observed in the middle corona. Due to a general prioritization of the lower solar atmosphere in EUV observations, the extended solar atmosphere was largely overlooked prior to SWAP.

The composition of the extended corona and what generates the emission from the region, especially in the middle corona, have long been debated (e.g. Del Zanna et al., 2018). However, a lack of in-situ or direct measurements has led to much speculation. The EUV emission $[E]$ is believed to be generated by a mixture of *collisional excitation* of ions by electrons ($E \propto n_e^2$), where n_e is the electron density, and *resonant scattering* of the monochromatic radiation generated in the underlying corona ($E \propto n_e$). As density decreases with height, the fall-off rate of collisionally excited emission is steeper than the rate of fall-off of resonantly scattered emission. At low heights, all emission is dominated by collisionally excited processes, but as height increases, the steep fall-off in this component of emission means that resonantly scattered emission becomes proportionally more important.

In contrast to the EUV emission in the lower solar atmosphere, the WL coronal emission is created by *Thomson scattering*, the scattering of photospheric continuum radiation by free coronal electrons ($E \propto n_e$) (see introduction of Goryaev et al., 2014, for a thorough discussion). This change in emission mechanism, combined with the temperature that generated the emission often makes it difficult to reconcile the fine structure of phenomena that extend from EUV to WL.

2.2. SWAP Observations and Image Processing

The SWAP nominal observing program is composed of ten-second, Sun-centered exposures made with a roughly two-minute cadence. However, PROBA2 also offers an adaptive off-point program, which has permitted several special observing campaigns (e.g. O'Hara et al., 2019), and allows SWAP to off-point by up to one degree, providing further imaging of extended coronal features, reaching the inner edge of WL instruments, such as the LASCO-C2 coronagraph on the SOHO spacecraft. Figure 3 shows a composite image constructed from 70 images obtained during the 26 November 2014 Mosaic campaign, comprised of 60 off-pointed and 10 Sun-centered images. The image highlights that EUV emission can be seen out to nearly 3 $R_\odot$ from the Sun center through the SWAP bandpass.

An important, higher-level, SWAP data product is *Carrington-rotation images*. These images combine multiple individual SWAP Level-1 images into a deep-exposure, high signal-to-noise, median-averaged image to make faint structures in the outer FOV visible. The individual input images are grouped in 100-minute intervals to ensure stacked images include some images from each of the four orientations of the spacecraft over the course of a full 90-minute orbit, which helps to eliminate positional anisotropy from the resulting stacked image.

At the edges of the SWAP images the data are dominated by temporal noise, which results primarily from uncorrectable dark and fixed-pattern noise, and cosmic-ray spikes, and is
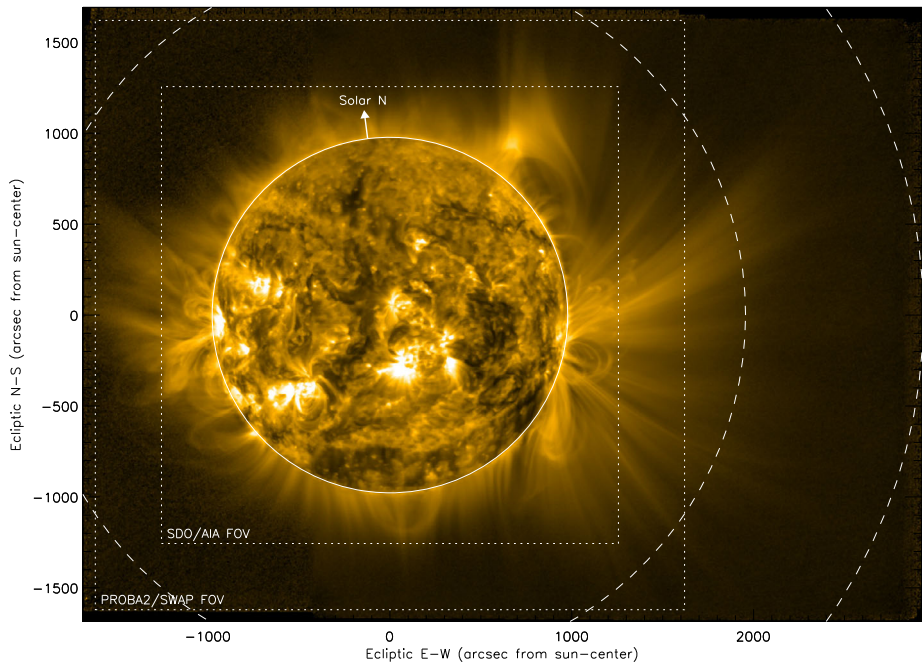
Figure 3 A composite image from the 26 November 2014 SWAP Mosaic campaign combining nominal and off-point observations, where the inner square indicates the AIA nominal FOV, and the outer square is the nominal SWAP FOV. The two circles indicate distances of 2 $R_\odot$ and 3 $R_\odot$ from the solar-disk center.

uncorrelated with the coronal signal. When stacking images in which the noise is correlated with the image (i.e. error arises primarily from photon shot noise) using the mean yields the best result, because the primary goal of stacking is to aggregate more counts to reduce the significance of the shot noise to the total image signal. When the noise is uncorrelated with the image, the primary goal is to suppress random variations and preserve the stable signal (the image), thus the median is more effective. The median also has the benefit of suppressing dynamics within the stacked images, resulting in an image that emphasizes the steady-state coronal features such as streamers and fans.

Stacked images are subsequently grouped into collections of images corresponding to Carrington-rotation periods (hence the name), and they can be found at proba2.sidc.be/swap/ data/carrington_rotations/. Users requiring non-standard image stacks can use the SWAP utility p2sw_long_movie.pro, included in the SWAP IDL software package in SolarSoft.

Figure 4 shows a comparison of a SWAP Carrington-rotation image (bottom panel), from 14 November 2014 at about 18:30 UT, to a nominal Level-1 image (top panel) near the center of the stack (18:27:36 UT). The median-stacked image is composed of 34 individual exposures obtained over the 100-minute image aggregation window. Both images have been processed with an azimuthally varying radial-normalizing filter (see the methods section in Seaton et al., 2021), developed specifically for these SWAP data products, which helps compensate for the large radial gradient from the solar limb to the edge of the FOV to reveal coherent structures across the entire image. When stacking (summing) images to enhance signal, fast-moving structures become smeared as they are recorded at different positions in successive images. If summed for long enough, the same is true for long-lived structures

Figure 4 A comparison of a single SWAP Level-1 image (*top*) with a corresponding median-stacked SWAP Carrington-rotation image (*bottom*), demonstrating how stacking SWAP data suppresses noise and reveals large, coherent structures in the corona that are too faint to be seen in single exposures.
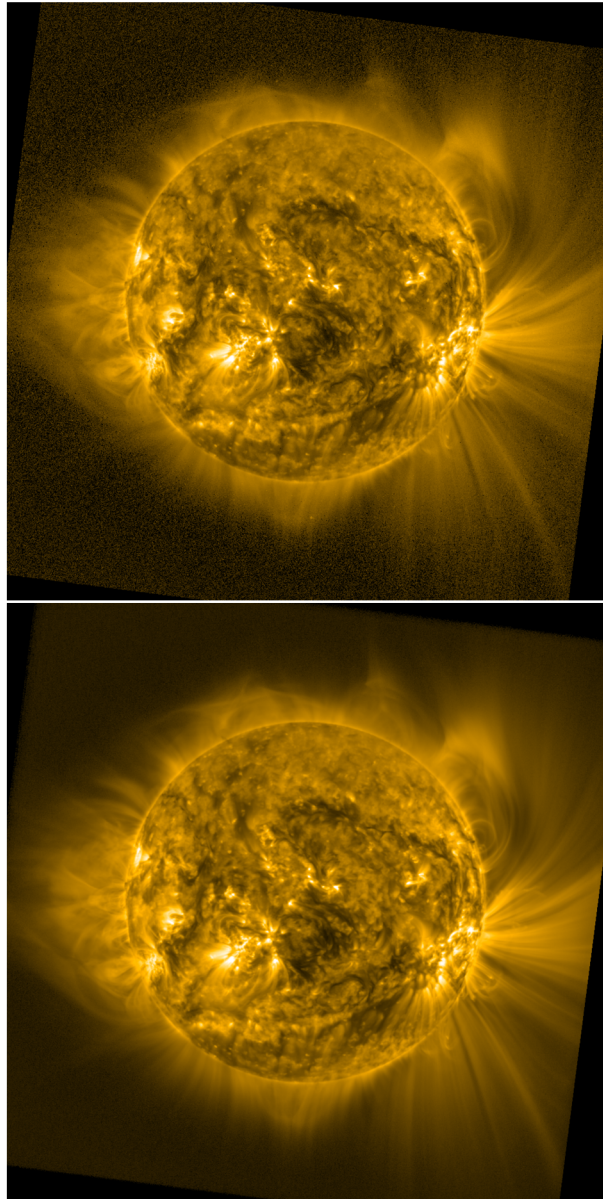
that corotate with the Sun, such as active regions as they cross the solar disk, and streamers in the extended solar atmosphere.

The optically thin nature of the solar atmosphere makes tracking structures difficult, due to projections and superimposed structures. On the solar disk, where the emission from the lower corona dominates, structures will roughly rotate across the solar disk at the solar rotation rate (with projection effects). Off the solar limb, the optically thin signal is composed of all observable emission along the line-of-sight, with the dominant emission in the plane of the sky. The projected signatures of structures close to the plane of the sky will appear to

move away from the Sun as they approach the plane of the sky, before moving back toward the Sun.

If we consider a hypothetical instrument, with a perfect point-spread function, no scattering or distortion, and where the emission recorded in each pixel is assumed to be located at the center of each pixel, we can estimate the time taken for a packet of plasma to rotate from one pixel to an adjacent pixel due to solar rotation. Figure 5 shows a contour plot of time taken for a feature to pass from one pixel to an adjacent pixel, where the dimensions and number of pixels correspond to those of SWAP. Structures on the solar disk are assumed to rotate at the differential rotation rate, and structures off-limb are assumed close to the plane of the sky and are crudely assumed to rotate as rigid bodies. The calculations required to make this plot are described in the Appendix.

Figure 5 shows that pixels in the extended corona can be stacked for longer periods, in an ideal case up to approximately five hours. However, this assumes that structures are close to the plane of the sky. The short rotation times on the solar disk imply structures will become smeared with extended stacking periods, even with the relatively short 100-minute stacks used to make the Carrington-rotation images. However, by using a median stack as opposed to a mean stack some of the smearing can be mitigated.

As EUV images of the corona contain information over a wide range of spatial and brightness scales, image-processing techniques have been developed to tease out this information. Morgan and Druckmüller (2014) developed a very efficient processing technique based on localized normalizing of the data at many different spatial scales, the Multiscale Gaussian Normalization (MGN) technique, revealing information at the finest scales while maintaining enough of the larger-scale information to provide context. Importantly for SWAP and the middle corona, MGN also intrinsically flattens noisy regions revealing structure in off-limb regions, out to the edge of the field of view. Morgan and Druckmüller (2014) successfully applied MGN to several datasets, including SWAP images (see Figure 7 in Morgan and Druckmüller, 2014), where the MGN-processed SWAP image from 31 August 2012 reveals the structure of an erupting filament out to the extremity of the FOV, and other quiescent structures to ≈ 1.5 R$_\odot$. Even low-signal structures are enhanced without too much amplification of noise. Figure 6 shows an example of the results of processing the stacked image shown in Figure 4 with an MGN filter to enhance structure over the FOV.

3. SWAP-Based Studies of Phenomena Observed in the Extended Corona

Structures observed in the extended EUV corona can be roughly divided into dynamic and long-lived phenomena, which are not necessarily mutually exclusive. Dynamic events rely on nominal-cadence observations to track fast-moving structures that pass through the off-limb corona on time scales of minutes to hours. These include: eruptions, flows, and blobs. In contrast, long-lived structures can persist for days to weeks, and include streamers, pseudo-streamers, and fans. The long-lived structures are well observed in Carrington-rotation images, which enhance persistent coherent structures, and are not smeared by the median-stacking process.

This section reviews all articles that have used SWAP to help investigate the extended EUV solar atmosphere and phenomena observed there. It has been broadly divided into two main sub-sections: i) a review of long-lived phenomena in Section 3.1; ii) a review of dynamic phenomena in Section 3.2.
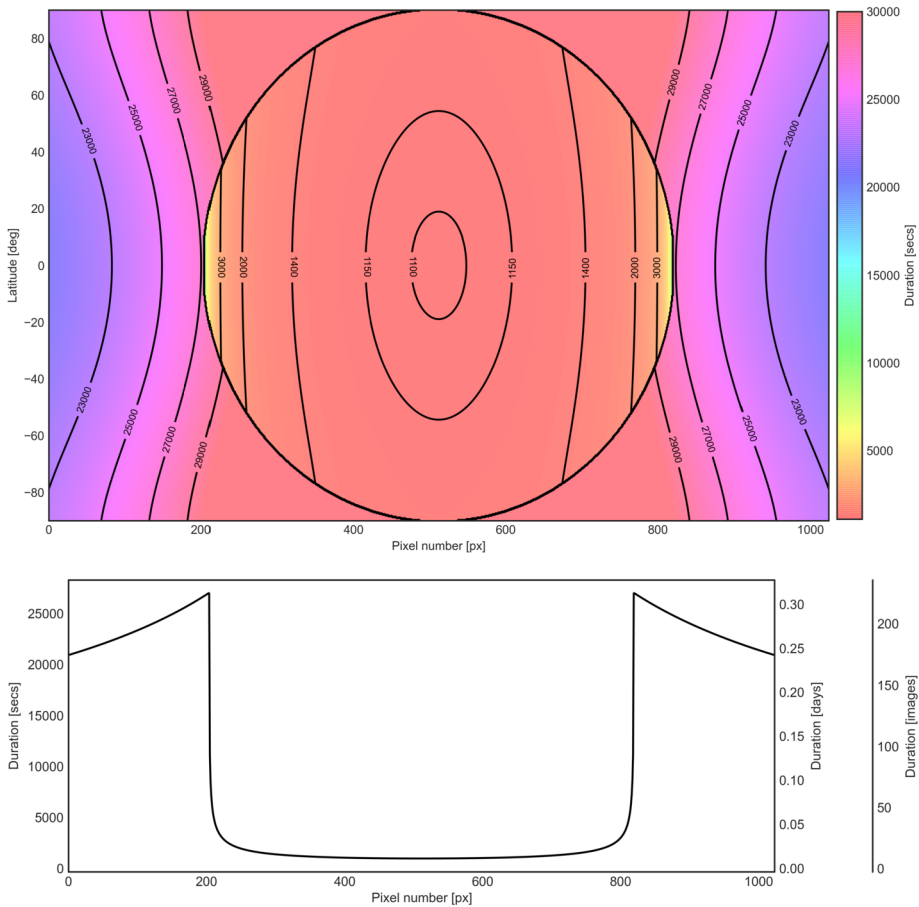
Figure 5 (*Top*) A contour plot of periods indicating the time taken in seconds for idealized emission to rotate from one SWAP pixel to an adjacent pixel due to differential rotation. The *dark circle* indicates the solar limb. Points within the solar limb rotate at the solar differential rotation rate, and those off-limb are assumed to rotate as rigid bodies in the plane of the sky. (*Bottom*) A slice through the 0 latitude of the contour plot, indicating the period of rotation in seconds, days, and number of successive SWAP images. See the Appendix for further details.

3.1. Long-Lived Phenomena

3.1.1. Streamers and Pseudo-streamers

Streamer-like structures have been studied for many years, and they are generally classified into two categories: (helmet) streamers and pseudo-streamers (Pneuman and Kopp, 1971; Wang, Sheeley, and Rich, 2007). As discussed by Rachmeler et al. (2014), a streamer is a magnetic structure overlying a single (or an odd number of) polarity inversion lines (PILs), whereas a pseudo-streamer is a magnetic structure overlying two (or an even number of) PILs. Both types of structures can also contain coronal cavities, tunnel-like areas of rarefied density, which possess a circular or elliptical cross section (Gibson and Fan, 2006).

Streamers are more traditionally observed in WL coronagraph observations as bright radial features extending out into the heliosphere; however, the lower coronal magnetic topol-

Figure 6 Stacked SWAP image from 14 November 2014, processed with the MGN filter (Morgan and Druckmüller, 2014).
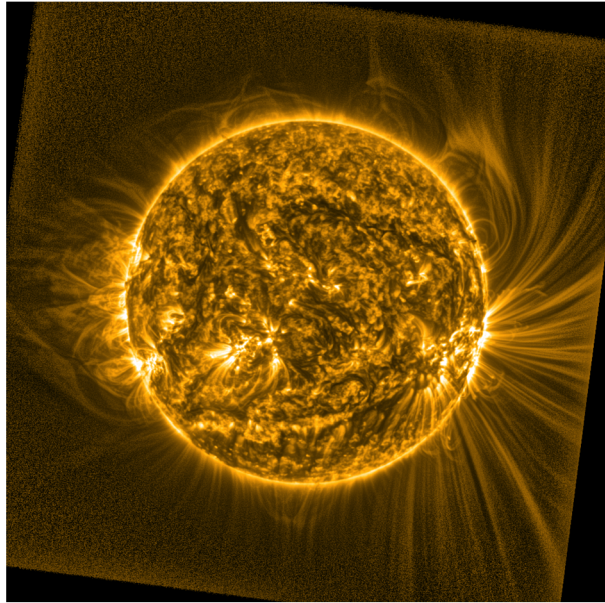
ogy cannot be discerned from such observations. Large-FOV EUV observations allow the magnetic topology to be traced from the lower corona out into WL observations, via the emission generated by the contained plasma.

Rachmeler et al. (2014) used SWAP with *Coronal Multichannel Polarimeter* (CoMP: Tomczyk et al., 2008) (1074.7 nm), and *Chromospheric Telescope* (ChroTel: Bethge et al., 2011) (Hα 656.3 nm) observations to investigate a streamer–pseudo-streamer observed between 5 and 10 May 2013, and reported on the first observation of a single hybrid magnetic structure that contained both a pseudo-streamer and a double-streamer structure. The structure consisted of a pair of filament channels, where a double streamer was located adjacent to one channel and a coronal pseudo-streamer (without a central open-field region) adjacent to the other. The structure could be traced out to the edge of the SWAP FOV, in the middle corona.

Guennou et al. (2016) used SWAP data to investigate a large-scale coronal pseudo-streamer/cavity system that was visible for approximately a year (February 2014 – February 2015). The authors used EUV tomography with both SWAP and AIA observations to probe the structure of the pseudo-streamer and to determine its 3D temperature and density structure using a differential emission measure (DEM: e.g. Plowman, Kankelborg, and Martens, 2013) analysis. Reconstructions of the observed pseudo-streamer showed the associated cavity to be less dense than the surrounding pseudo-streamer, and the volume enclosed within to be systematically hotter than the surrounding plasma.

During the 11 July 2010 eclipse, Pasachoff et al. (2011) drew comparisons between ground-based WL eclipse observations and SWAP observations of a streamer structure. The streamer appeared bright in WL observations, but in contrast it appeared as a void in the corresponding SWAP observations. Using observations from the hotter AIA 19.3-nm passband, the authors were able to determine that the streamer was largely emitting at higher temperatures, and it was therefore largely invisible in the cooler Fe IX and Fe X lines observed by SWAP.
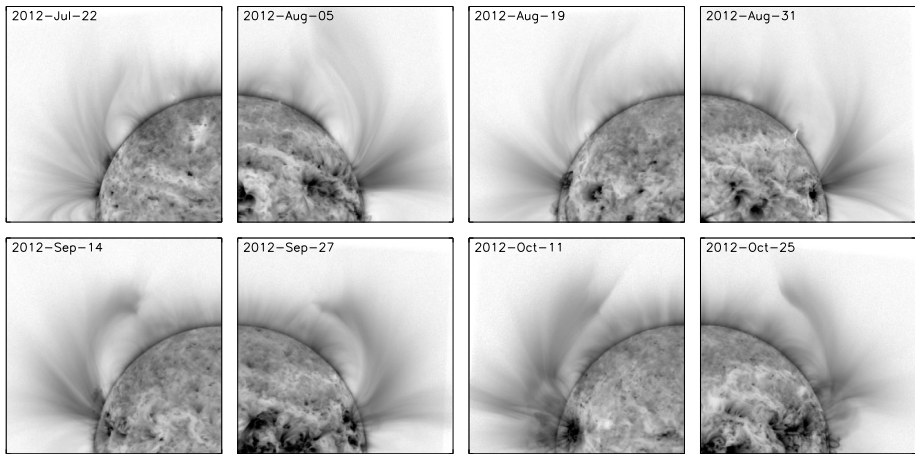
Figure 7 Inverse-color image of the long-term evolution of a large, fan-shaped structure that persisted for several solar rotations in 2012. (Figure 8 from Seaton et al., 2013a, used with permission).

3.1.2. Coronal Fans

Coronal fans are large-scale extended structures observed off the solar limb in EUV and WL observations (see, e.g., Koutchmy and Nikoghossian, 2002; Morgan and Habbal, 2007, and references therein). They are often observed to be composed of open magnetic fields that overlie polar-crown filaments and extend out into WL observations. Seaton et al. (2013a) used SWAP observations over a three-year period to study the evolution of the extended EUV corona during the rise of Solar Cycle 24. Their analysis indicated that coronal fans can persist for many solar rotations, they are the single largest source of brightness at heights above 1.3 R$_\odot$, and they are closely associated with the appearance of active regions at lower heights. Mierla et al. (2020) also showed that fans can last for extended periods of time, and in particular observed one fan for more than 11 Carrington rotations (from February 2014 to March 2015), which could be seen extending out to 1.6 R$_\odot$.

Fans are typically associated with active regions and periods of increased solar activity. They appear to be predominantly open features, which bend over large, closed loops, before extending outwards (Mierla et al., 2020). Figure 7, from Seaton et al. (2013a), shows the long-term evolution of such a fan-shaped structure. A cusp-shaped void, indicative of a prominence cavity, is often observed beneath the curve of a fan. SWAP observations indicate that the structures of fans are sheet-like, in that they extend along a particularly deep line of sight, which can be seen as they rotate around the solar limb. Sharply defined boundaries are seen at the interface between the fan structure and adjacent closed magnetic field. Seaton et al. (2013a) hypothesized that the nearby closed magnetic-field structures are not visible in SWAP observations due to being too hot to be observed in the 17.4-nm passband.

Fan structures are almost always associated with small, long-lived regions of activity, near the edges of the closed-field region that the fan overlies (Seaton et al., 2013a). These small regions appear to be the footpoints of the fan structure and are observed as brightenings with SWAP. The evolution of 15 fans observed by SWAP between March 2010 and July 2010, and during a second period between July 2012 and October 2014, is discussed by Mierla et al. (2020). The footpoints of the fans were always found within the interval [−40°, 40°] latitude, indicating a correlation with active latitudes, although they found that

only half of the fans could be associated with large active regions. For most of the fans considered, the footpoints remained within the same magnetic domain, meaning that they were unipolar. Nearly half of the footpoints were located close to coronal holes, but none were found within a coronal hole. Mierla et al. (2020) focused on the off-limb EUV-intensity variations of a particularly long-lived fan from the study, which persisted for more than 11 Carrington rotations. From this, they estimated the rotation rate of the fan to vary between 10 and 15° per day, with an average of 12.45° per day. They hypothesized that this variation in rotation rate could indicate that a fan is not rigidly anchored to its photospheric footpoints, or that some coronal phenomena could affect the rotation rate. They cautioned, however, that the EUV-intensity variations could also result from the superposition of many features when integrating along the line of sight.

An important question is the extent to which fans can be associated with streamers and pseudo-streamers. In some cases, there does appear to be evidence of a relationship between these features. Seaton et al. (2013a) presented an example where the void beneath the fan structure appears to have a double-lobe shape, which is consistent with the base of a pseudo-streamer. This is backed up by the magnetic structure obtained through a potential-field source-surface (PFSS: Schrijver and De Rosa, 2003) extrapolation, which they compared with the SWAP observations. Further, a cusp-shaped feature associated with a sequence of filament eruptions was observed by SWAP in August 2010. Modeling by Titov et al. (2012) indicated that such structures can be associated with pseudo-streamers. Seaton et al. (2013a) also discussed other cases, however, where it is less obvious if there is a relationship between a fan and pseudo-streamer. They point out that fan structures appear to be more localized than either streamers or pseudo-streamers, with the latter two often extending out into the heliosphere.

On the other hand, Mierla et al. (2020) discussed that fans can be associated with both streamers and pseudo-streamers. They found that structurally, if a fan appears to have a "knee" (an abrupt bend, see panel labeled "2012-Oct-11" in Figure 7) then it most likely overlies a pseudo-streamer, whereas those lacking a knee are more likely associated with a streamer.

Meyer et al. (2020) simulated the global coronal magnetic field out to 2.5 $R_\odot$ from 1 September 2014 to 31 March 2015 using a continuous, time-evolving, nonlinear force-free field model (see Section 3.1.4). They compared the simulated coronal magnetic field with co-temporal observations from SWAP of a fan that persisted for five Carrington-rotations. It was observed that the simulated magnetic-field structure in the vicinity of the fan changed from a streamer configuration to a double-lobed pseudo-streamer configuration between the second and third rotations.

3.1.3. Prominences and Cavities

Prominences, also called filaments when observed in absorption on-disk (we will use both terms interchangeably in this article), are large structures observed in the extended EUV atmosphere. They are often modeled as twisted magnetic-flux ropes (Gibson and Fan, 2006), and they can contain plasma two orders of magnitude cooler and denser than the average background corona, and as such they can appear dark in several EUV passbands, including SWAP. Prominences can dissipate in several ways, including slow decay, or through a dynamic instability. A more violent phenomenon is the prominence eruption, resulting from the explosive rearrangement of the magnetic structure, and its ejection into the extended corona (Parenti, 2014).

Observations of prominences at the limb often reveal a darker region, a coronal cavity, extending above and around a prominence up to around 1.6 R$_\odot$ (Parenti, 2014). In magnetic-flux-rope models, the filament and cavity are described as two parts of the same magnetic structure, where the cavity is the upper coronal part of a filament channel (Gibson et al., 2010). Cavities are believed to be the density-depleted cross sections of the magnetic-flux ropes, where the magnetic-field strength has attained greater values than the background corona (Rachmeler et al., 2013).

Bazin, Koutchmy, and Tavabi (2013) compared off-limb SWAP observations of a couple of prominence and cavity structures to simultaneous, slitless flash spectra obtained during the total solar eclipse of 11 July 2010. The flash spectra (see description by Bazin, Koutchmy, and Tavabi, 2013) were used to measure the continuum emission outside the prominences, and to study the electron density of the cavity. Intensity deficits were observed and measured at the boundaries of cavities in both eclipse and SWAP images. Bazin, Koutchmy, and Tavabi observations also tend to confirm earlier results reported by Harvey (2000) that cavities are hot plasma inside the filament channels.

Quiescent prominences, when viewed at the limb, often appear as curtains of vertical, thread-like structures (Berger et al., 2008). Occasionally, they have the appearance of tornadoes, composed of rotating magnetic structures. As described by Panesar, Innes, and Tiwari (2013), the driving mechanism for this rotation is not resolved, but it is often attributed to a coupling and expansion of a twisted flux rope into the coronal cavity (Liu et al., 2012) and/or can be related to photospheric vertices at the footpoint of the tornado (Attie, Innes, and Potts, 2009).

Panesar, Innes, and Tiwari (2013) used a combination of SWAP and AIA observations to investigate the triggering mechanism of a solar tornado observed in a prominence cavity close to the solar limb around 25 September 2011. A neighboring active region produced three eruptive flares, with associated coronal waves. Panesar, Innes, and Tiwari (2013) suggest the magnetic reconfiguration may have affected the cavity–prominence system triggering the solar tornado, where the active-region coronal field contracted by the Hudson effect (Hudson, 2000) through the loss of magnetic energy via flares. As a consequence, the cavity expanded due to its magnetic pressure, filling the surrounding corona, and the tornado was the dynamical response of the helical prominence field to the cavity expansion.

3.1.4. Structural Evolution of the Extended Atmosphere

The first-ever study of the evolution of the large-scale EUV corona, over a three-year period between February 2010 and December 2012, which included the complete rise phase of Solar Cycle 24, was made by Seaton et al. (2013a). Using carefully processed images with stray light removed, and applying techniques similar to those used to construct the Carrington-rotation images, described in Section 2.2, Seaton et al. (2013a) produced high signal-to-noise composites that revealed the structure of the large-scale EUV corona to relatively large heights. Similar techniques were used by Mierla et al. (2020) to extend the study throughout the whole of Solar Cycle 24 (from 2010 to 2019).

By comparing the EUV signal at different heights with international sunspot number (ISN: SIDC – sidc.oma.be/silso/datafiles), both Seaton et al. (2013a) and Mierla et al. (2020) show the growth of the complexity and extent of the EUV corona at large heights are closely correlated. In particular, the inner corona was linked to rising activity in the extended corona through the development of long-lived, extended structures (coronal fans, see Section 3.1.2), which were observed to persist over many solar rotations. Figure 8, which is taken from Seaton et al. (2013a), shows both the sunspot number and extended SWAP EUV emission
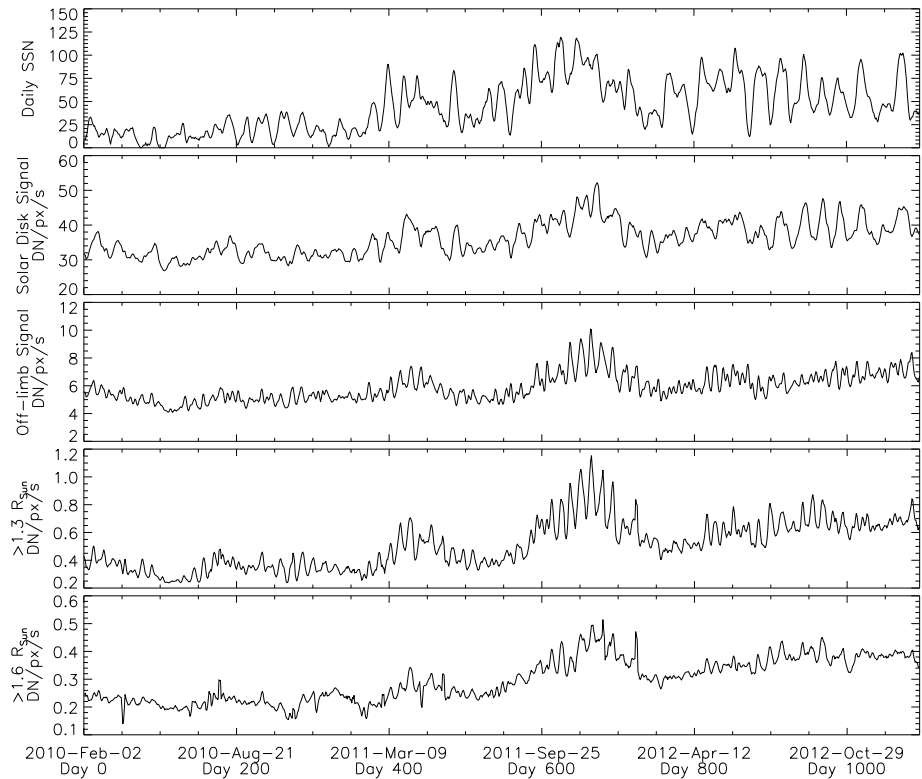
Figure 8 Sunspot number (SSN) and EUV signal as a function of time from February 2010 to December 2012. The *top panel* shows the SSN, the *second panel* shows the on-disk EUV signal measured by SWAP, and the *subsequent panels* show the mean off-limb brightness above 1 R$_\odot$, 1.3 R$_\odot$, and 1.6 R$_\odot$, respectively. (Figure 6 from Seaton et al., 2013a, used with permission).

as a function of time. The figure highlights the correlation between growing sunspot number (SSN) and EUV emission, and a strong periodicity due to the appearance and disappearance of bright structures as a result of solar rotation. Seaton et al. (2013a) note a lack of understanding as to the source of brightness in coronal structures at large heights (see discussion in Section 2.1).

The study of Mierla et al. (2020) was able to draw comparisons of extended structures over a whole solar cycle, where it is noted that peaks in EUV averaged intensity were observed at both poles in the descending phase of Solar Cycle 24, which appear to be associated with the start of the development of polar coronal holes. It is also noted that large-scale off-limb structures were largely absent around the solar-minimum phase of solar activity. Mierla et al. (2020) also analyzed the rotation rate of bright structures at three latitudes: $+15°$, $0°$, and $-15°$, and found a consistent rotation rate of around 15° per day.

To study and validate the modeling of extended coronal structures that transcend the extended corona, Meyer et al. (2020) compared SWAP observations to a global non-potential magnetic-field simulation, which uses a magneto-frictional method (see, e.g., Yeates, Mackay, and van Ballegooijen, 2008; Yeates et al., 2018). The simulation, driven by newly emerging bipolar active regions determined from *Helioseismic and Magnetic Imager* (HMI: Schou et al., 2012) magnetograms, produces a continuous evolution of the coronal

magnetic field through a series of nonlinear, force-free equilibria, which allows the build up of magnetic connectivity, electric currents, and free magnetic energy in the simulation (see references within Meyer et al., 2020).

The Meyer et al. model assumes that under the low-β assumption the plasma is dominated by the magnetic structures that contain it, and thus the solar atmosphere is highly structured. By studying the period from 1 September 2014 to 31 March 2015, around a solar maximum, when there were extensive bright and extended structures, they were able to show that the model was capable of accurately reproducing observed large-scale, off-limb structures. In particular, they showed that the model was capable of replicating the evolution of a coronal fan observed over several rotations. Comparisons were also drawn with a cavity/pseudo-streamer structure at the South Pole (Guennou et al., 2016), where an observed decrease in height over time was also captured by the simulation, although the simulation does not produce the correct scale of the structure. Such simulations allow further long-term exploration of the extended EUV atmosphere.

3.2. Dynamic Phenomena

3.2.1. Eruptions and Jets

Solar eruptions are the largest and most dynamic phenomena produced by the Sun (e.g. Webb and Howard, 2012; Zhang et al., 2021). These eruptions of magnetized solar plasma can propagate into interplanetary space at speeds up to thousands of $km\,s^{-1}$ (e.g. Yashiro et al., 2004). When Earth directed, they can lead to geomagnetic storms upon impact with the Earth's magnetosphere. As a consequence, understanding the physics and kinematics of eruptions has been at the forefront of heliophysics and space-weather research for many years (Temmer, 2021).

Solar eruptions are described as emerging in three phases: an initiation (or *gradual*) phase that generally occurs in the lower corona $< 2\,R_\odot$, an impulsive acceleration phase through the lower and middle corona where the eruption undergoes the most dramatic acceleration, and a propagation phase (e.g. Zhang and Dere, 2006) where the eruption approaches a constant (cruise) speed, or acceleration. The first two phases are dictated largely by the Lorentz force, while the third phase, as the CME propagates through the outer corona and heliosphere, is mainly dictated by the drag force (e.g. Cargill et al., 1996). Many CMEs consist of a three-part structure: a bright ejecta front, a dark cavity, and a bright core. Faster eruptions can develop a shock front ahead of the ejecta front (e.g. Zhang and Dere, 2006).

Typically, an eruption is believed to be initiated by an ideal magnetohydrodynamic (MHD) instability and/or magnetic reconnection. As a consequence, most eruptions are associated with flaring activity (sometimes referred to as eruptive flares). Beyond the initiation phase, the eruption is mainly influenced by the background corona/solar wind (e.g. Schrijver et al., 2008; Mierla et al., 2013; O'Hara et al., 2019), especially in the relatively dense lower and middle coronal regions, where an eruption's kinematics are shaped and it undergoes its main acceleration phase. The large FOV of SWAP has provided several authors the opportunity to track eruptions through this critical phase.

The formation and eruption of six limb events observed with SWAP, AIA, and LASCO, between June 2010 and June 2011, were studied in a series of articles by Fainshtein and Egorov (2013), Egorov and Fainshtein (2013), Fainshtein and Egorov (2015). In Fainshtein and Egorov (2013) two classes of CME, separated by their velocity profiles, were identified. The first includes eruptions whose velocity reaches a maximum before sharply dropping by $> 100\,km\,s^{-1}$ into a regime of slow change. The second class includes eruptions whose
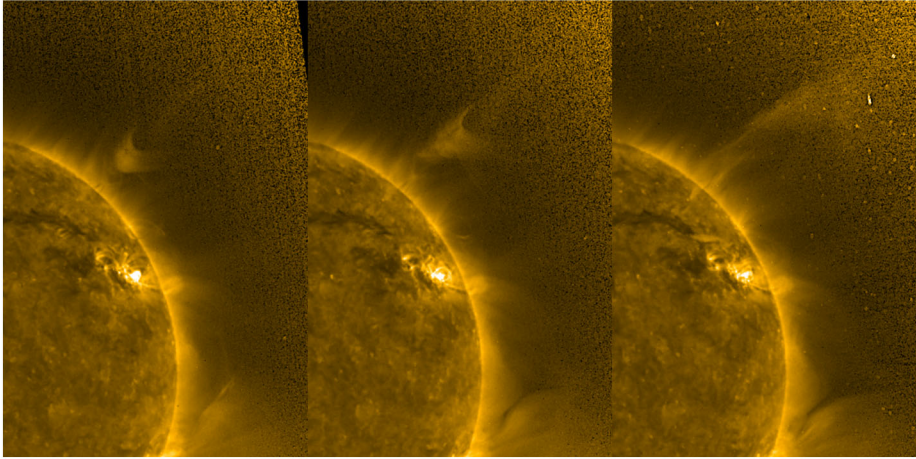
Figure 9 Successive SWAP images of the cavity eruption observed on 13 June 2010 at ≈06:00 UT, ≈07:00 UT, and ≈08:00 UT studied by Sarkar et al. (2019).

velocity changes slowly immediately after reaching a maximum. All eruptions exhibited rapid expansion phases in the early stages of their development. Egorov and Fainshtein (2013) and Fainshtein and Egorov (2015) also discussed the finding that associated shocks show a self-similar motion, leading the authors to conclude that the shocks were not driven by a piston-like action.

A filament eruption observed on 5 May 2015 was tracked from the lower corona out through the heliosphere using a variety of instruments by Johri and Manoharan (2016). The CME underwent rapid acceleration and expansion through the lower and middle corona (up to ≈ 6 $R_\odot$), before settling at a speed ≥ 800 km s^{-1}. The initiation and near-Sun signatures, located < 2 $R_\odot$, were tracked using off-limb SWAP and AIA observations. Further out, interplanetary-scintillation (IPS) measurements obtained from the *Ooty Radio Telescope* (ORT: Swarup et al., 1971) at 327 MHz, were used to track the eruption and ambient solar wind. This particular eruption was observed to interact with a preceding slower CME. This interaction, which led to increased turbulence levels, was captured in solar-radio-dynamic spectra obtained from the *Hiraiso Radio Spectrograph* (HiRAS) and the WAVES radio experiment onboard the *Wind* spacecraft (Bougeret et al., 1995).

Sarkar et al. (2019) studied the evolution of an erupting cavity/prominence structure from its quiescent state (between 30 May and 13 June 2010) through its eruptive phases using EUV observations from multiple vantage points and observatories, including SWAP, AIA, and EUVI. Prior to eruption, the quiescent cavity went through a sequence of quasi-static equilibria, which exhibited a slow rise and an expansion phase. By comparing the decay index of the cavity system during the different phases, Sarkar et al. found that, assuming the eruption was triggered by a torus instability, the magnitude of the decay index at the cavity-centroid height is a good indicator to predict an eruption. Figure 9 shows successive images of the 13 June 2010 cavity eruption studied by Sarkar et al. (2019).

Combined observations from SWAP and LASCO were used by Sarkar et al. (2019) to track the evolution of the cavity (EUV observations) into the three-part structure of the associated CME (WL observations), that was observed on 13 June 2010. The kinematic study captured both the impulsive and residual phases of acceleration along with a strong deflection. By successively fitting the cavity with an expanding ellipse, they found that the

cavity exhibited non-self-similar expansion (the ratio of the major to the minor axis of the ellipse did not increase linearly with height) in the low and middle corona, below $2.2 \pm 0.2\,R_\odot$, which resembles the radius of the source surface ($2.5 \pm 0.25\,R_\odot$) where the coronal magnetic-field lines are believed to become radial (Hoeksema, 1984).

In contrast to the larger events described above, small filament-channel outbursts can form smaller eruptions, or *coronal jets* (e.g. Sterling et al., 2015). Magnetic-flux ropes reconnect low in the corona, transferring magnetic twist and filament plasma to the surrounding open field. This creates a narrow plasma ejection that adds no new open flux to the heliosphere, unlike larger eruptions that can remain connected to the surface.

As discussed by Wyper et al. (2021), the unifying feature of all these eruptions are filament channels. They are strongly sheared magnetic-field lines that follow PILs, and they can provide the free magnetic energy for the eruption. One important aspect dictating how a filament erupts, is its interaction with the surrounding magnetic-field topology, as this strongly affects how the eruption is triggered, the kinematics, trajectory, and morphology of the event.

Wyper et al. (2021) present a numerical simulation of a new type of coupled eruption, in which a jet initiated by a large pseudo-streamer/filament eruption triggers a sympathetic streamer-blowout CME from a neighboring helmet streamer. Wyper et al. used SWAP observations from 24 July 2014 to provide evidence of such a pseudo-streamer harboring a small filament observed on the limb. The pseudo-streamer topology resembled that of a single null point above two coronal arcades, which sit between coronal holes of like polarity (see Figure 1 in Wyper et al., 2021). This multi-polar topology shows that pseudo-streamers can host filament eruptions that occur via magnetic breakout.

Alzate and Morgan (2016) applied the MGN technique (see Section 2.2) to observations from several instruments to help track a series of fast eruptions, or puffs, over the course of a three-day period starting on 17 January 2013. As part of this study they focused on an intermittent eruption that had a very gradual initial phase and was linked to a series of fast eruptions. The eruption was faint in EUV observations, but it could be tracked through the SWAP FOV (see Figure 3 in Alzate and Morgan, 2016), linking it to structures in WL coronagraph observations.

3.2.2. Eruptions: Bridging the Observational Gap

Tracking the early phases of an eruption using space-based instrumentation along the Sun–Earth line has proved challenging, as the transition from the main acceleration to the propagation phase often occurs between the inner corona (EUV observations) and the outer corona (WL observations) (Byrne et al., 2014; D'Huys et al., 2017; Reva et al., 2017). As a consequence, the larger FOV of SWAP has been used in multiple publications to explore the early stages of eruptions, especially in combination with surrounding LASCO WL observations. However, even with the wider FOV, a gap still exists between the outer edge of SWAP observations and the inner edge of LASCO observations, as can be seen in the top panel of Figure 10.

One method of bridging the observational gap using SWAP involves the use of observations made during periods when the PROBA2 platform was off-pointed, increasing the extended EUV FOV in a particular direction. O'Hara et al. (2019) tracked two eruptions, observed on 1 and 3 April 2017 near the western solar limb, while SWAP was off-pointed to the solar west by 495 arcsec, as part of an international campaign for coordinated observations (HOP 334: www.isas.jaxa.jp/home/solar/hinode_op/hop.php?hop=0334). A SWAP and LASCO composite image made during this campaign can be seen in the bottom panel of Figure 10. O'Hara et al. (2019) used these unique observations to directly trace the eruptions

Figure 10 A Sun-centered SWAP image from 1 June 2014 overlaid on top of a corresponding LASCO WL image (*Top*), highlighting the observational gap between nominal EUV and WL images. The *bottom panel* shows a SWAP image from 1 April 2017 off-pointed to the West, bridging the observational gap.
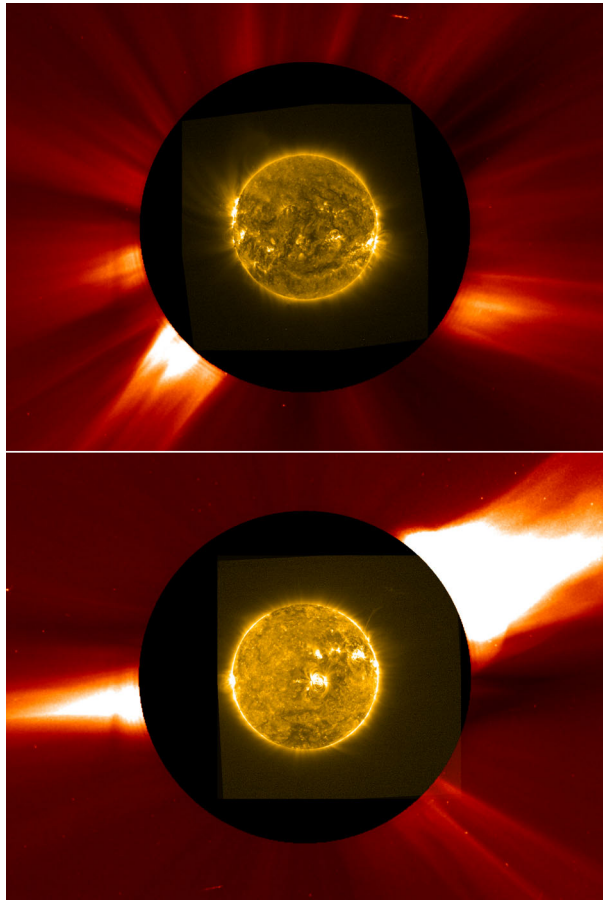
from EUV observations (ending at approximately 2.5 R$_\odot$) into WL LASCO coronagraph observations. It is discussed that although the overarching kinematics could be matched between the EUV and WL datasets, exact features were difficult to reconcile due to the different passbands.

Although the eruptions described by O'Hara et al. (2019) were produced by the same source region, they had very different kinematic profiles. The first eruption was more energetic and showed a clear deceleration as it transitioned into coronagraph observations, whereas the second eruption, although associated with a larger flare, was slower and exhibited less deceleration, suggesting the eruption did not have such an energetic initiation. The deceleration is believed to be caused due to a mixture of Lorentz, gravity, and drag forces created by the ambient corona and solar wind.

A few explanations are postulated as to why the initiation phases of the eruptions observed were so different from one another, including: different destabilization mechanisms, different amounts of available free energy, or varying background conditions. The differences observed between these two seemingly similar eruptions highlight the need for further exploration of the early phases of eruption dynamics in the extended EUV corona.

Byrne et al. (2014) used SWAP observations combined with WL imagery from the ground-based *Mark-IV K-coronameter* (Mk4: Elmore et al., 2003) to bridge the observa-

tional gap between AIA and LASCO observations. In contrast to the observations shown by O'Hara et al. (2019), which increased the EUV FOV to bridge the observational gap, the Mk4 observations, which are made between $1.1 - 2.8$ R$_\odot$, decreased the height of the WL observations to bridge the gap. The observations were co-aligned to study the initiation phase of an eruption observed on 8 March 2011, and multi-scale techniques (Young and Gallagher, 2008) were applied to improve the signal-to-noise. Byrne et al. found the eruption to be driven by a rising flux-rope structure from a *two-stage* flaring event located under a helmet streamer. The initial outward motion of the erupting loop system coincided with a flare peak, and it led to a plasma pile-up, which became the CME core material. The acceleration of the CME core then further increased, coinciding with a second flare peak, and it expanded into an overlying streamer (see Figure 4 in Byrne et al., 2014). It was concluded that the formation of either a kink-unstable or torus-unstable flux rope was the most likely cause of the eruption.

Similar to Mk4 (and, subsequently, KCor) observations, ground-based eclipse observations have provided other unique opportunities to overlap WL (and other passbands that can penetrate Earth's atmosphere) observations with nominal SWAP observations. Eclipse observations have less stray-light issues than conventional coronagraphs, and they can generally reach far lower heights, even overlapping EUV observations. Example campaigns include those presented by Pasachoff et al. (2011, 2015), where WL eclipse observations were combined with SWAP and AIA observations to create composite images and trace structures from on-disk sources out to several solar radii (e.g. see Figure 14 of Pasachoff et al., 2015).

Pasachoff et al. (2011) used observations from the 11 July 2010 eclipse to analyze and contrast signatures of coronal holes, streamers, polar rays, faint loop structures, an eruption, and a puzzling *curtain-like* object above the North Solar Pole. Some structures were clearly visible in the WL observations but did not appear in SWAP imagery. The disparities were mainly attributed to differences between the density of the emitting structure and that of the surrounding corona. As the intensity of EUV emission scales with the density squared, in contrast to WL images, where intensity scales linearly with density, although the temperature of the emitting structure is likely to have contributed to the disparity as well.

Observations from the 13/14 November 2012 total-solar-eclipse campaign were presented by Pasachoff et al. (2015), where large-FOV WL, SWAP, and AIA composite images were used to trace structures out into the middle corona. During this campaign a weak eruption was captured in both WL and EUV observations. In particular, Pasachoff et al. (2015, Figure 17) showed a series of SWAP running-difference images highlighting the evolution of an eruption both on-disk and off-limb. By tracing the leading edge of the eruption, the authors estimated the speed through the lower and middle corona to be 413 km s^{-1}.

3.2.3. Eruptions: Multiperspective Tracking and 3D Reconstruction

As discussed in Section 2, the STEREO mission (Kaiser et al., 2008) is comprised of twin solar-observing spacecraft, which were launched into orbits around the Sun that cause them to orbit increasingly ahead of the Earth (STEREO-A) and behind the Earth (STEREO-B). Each STEREO/SECCHI suite of instruments contains a large-FOV EUV imager (EUVI), as well as COR-1 and COR-2 coronagraphs and the HI-1 and HI-2 *Heliographic Imagers* (Eyles et al., 2009). The mission has enabled multiple stereoscopic studies, in particular of eruptions and other large-scale structures extending into the heliosphere. The comparable FOVs of SWAP and the EUVI instruments have led to multiple joint studies between these instruments.
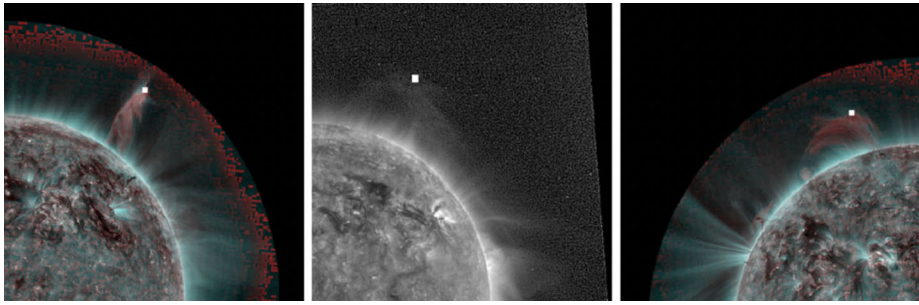
Figure 11 *Left and right panels*: EUVI (STEREO-B, and STEREO-A, respectively) images of prominence material observed on 13 April 2010. *Middle panel*: The corresponding prominence observed by SWAP. The center of the *white square* indicates the location where 3D reconstruction was performed and back-projected onto the 2D images (see Mierla et al., 2013, for further details). (Figure 1 from Mierla et al., 2013, used with permission).

Observations of the initiation phase of an eruption can provide clues about the forces acting on it. However, observations made from a single perspective may be misleading due to projection effects biasing measured kinematics. Therefore, several studies have tried to constrain the kinematics of an eruption using multiple viewpoints. Mierla et al. (2013) performed such a study of a prominence eruption observed on 13 April 2010, by combining the large FOVs of the SWAP and EUVI instruments, which in that period were separated by $\approx 70°$. Mierla et al. identified features in the prominence from the different perspectives and triangulated the positions to ascertain the true direction of propagation and the acceleration profile. By tracking the eruption they were able to show that the acceleration increased smoothly, and they concluded that the prominence was not accelerated *immediately* by local reconnection, but it was swept away as part of a large-scale relaxation of the coronal magnetic field. Figure 11, from Mierla et al. (2013), shows images from SWAP and the EUVI instruments of the 13 April 2010 prominence at around 08:15 UT, with the location where 3D reconstruction was performed and back-projected onto the 2D images.

A combination of SWAP, AIA, LASCO, and the SECCHI suite of instruments were used by Filippov, Koutchmy, and Tavabi (2013) to perform a multi-wavelength and multi-viewpoint study of a jet observed on 7 April 2011, originating from an active-region complex. The observations revealed an *Eiffel Tower* type configuration extending into a narrow jet in the outer corona, when observed from the Earth perspective. The event was observed to start growing following a failed cavity/flux-rope eruption (see Section 3.2.8). The resulting magnetic configuration corresponded to a saddle-like shape, providing the possibility for the plasma to escape along the overlying open field lines into the outer corona, forming the WL jet. The large FOV of SWAP helped provide evidence of the connectivity between the inner coronal structures and the corresponding outer coronal features observed by LASCO.

D'Huys et al. (2017) studied a fast ($v > 900$ km s^{-1}) wide-angled eruption observed on 14 August 2010, produced by an atypically weak (C4.4) flare. The eruption occurred near the west solar limb from the Earth's perspective, but it was clearly observed from all view points. The unwinding of the associated destabilized filament gave the eruption the appearance of an untwisting motion. D'Huys et al. examined the eruption with multiple instruments from both the Earth and STEREO perspectives, as well as with ground-based radio observations. Three-dimensional (3D) reconstructions were made using the epipolar geometry (Inhester, 2006) of the eruption, measured between SWAP and STEREO-A/EUVI 19.3-nm observations. SWAP was utilized to track the eruption off of the west solar limb

from the Earth perspective. Combined with coronagraph observations, they were able to extend this out to 10 R$_\odot$ (see Figure 13 in D'Huys et al., 2017).

The eruption clearly passed through different acceleration regimes, where the flux rope initially rose with a very low velocity and with a small amount of acceleration, before getting accelerated as it erupted catastrophically (between approximately 1.25 and 2 R$_\odot$), and finally it propagated with a near-constant, high velocity out through the heliosphere.

Seaton et al. (2011) also used a combination of SWAP and SECCHI observations to look at the three-dimensional structure of an eruption (observed on 3 April 2010), located at the disk center from the perspective of SWAP. The eruption occurred in two parts, with an initial flow of cooler material in the lower corona, followed by a flux-rope eruption in the higher corona. It is discussed that *mass off-loading* possibly led to the rise and loss of equilibrium of the flux rope (see Priest and Forbes, 2002).

Another multi-point study was performed by Witasse et al. (2017), but this time to track a large interplanetary coronal mass ejection (ICME) that was ejected from the Sun on 14 October 2014, not towards Earth, but throughout the Solar System. It was observed to hit Mars on 17 October, by the *Mars Express*, *Mars Atmosphere and Volatile EvolutioN* Mission (MAVEN), *Mars Odyssey*, and *Mars Science Laboratory* (MSL) missions, and possibly beyond. The ICME was also detected by STEREO-A on 16 October at 1 AU and by *Cassini* in the solar wind around Saturn on 12 November at 9.9 AU.

The multispacecraft observations helped Witasse et al. derive the early properties of the ICME, such as its angular extent (116°), its speed as a function of distance, and its magnetic-field structure at four locations from 1 to 10 AU. SWAP characterized the post-eruptive arcades (described by West and Seaton, 2015) observed in the wake of the eruption, and the observations from SWAP, AIA, and EUVI (which was located on the backside of the Sun from the perspective of the Earth) helped Witasse et al. (2017) constrain the source and early direction of the eruption.

3.2.4. Eruptions: Shocks and Particle Acceleration

The locations and mechanisms of particle acceleration generated during flares and eruptions are still subject to much investigation. Observing particle-acceleration sites can help confirm how the flare and eruption are initiated and how they evolve (Carley, Vilmer, and Gallagher, 2016). Radio imaging combined with metric and decimetric radio spectrography can be used to identify the sites of electron acceleration during an eruption. Beams of electrons can generate different radio signatures: two of the most common are Type-II radio bursts, which are believed to be generated by shock-accelerated electrons, and Type-III radio bursts, which are believed to be produced by fast flare-accelerated electron beams (see, e.g., Reid and Ratcliffe, 2014, for a review). Type-IV radio bursts are believed to be generated by electrons that are trapped inside CME loops, producing gyro-synchrotron emission. However, they are rarely observed in the extended solar atmosphere. If detected, these bursts can be used with numerical models to probe the source magnetic-field strength.

A flare and erupting flux rope observed on 18 April 2014 were studied by Carley, Vilmer, and Gallagher (2016), combining SWAP, AIA, and LASCO observations with radio dynamic spectra from the *Nançay Decametric Array* (NDA: Lecacheux, 2000) (between 10 – 80 MHz), and observations from several other instruments. Their analysis showed evidence of a slowly rising flux rope becoming destabilized co-temporally with the occurrence of a C-class flare, a plasma jet, and the escape of $\gtrsim$75 keV electrons, where various particle-acceleration sites were located throughout the eruption. LASCO and SWAP observations
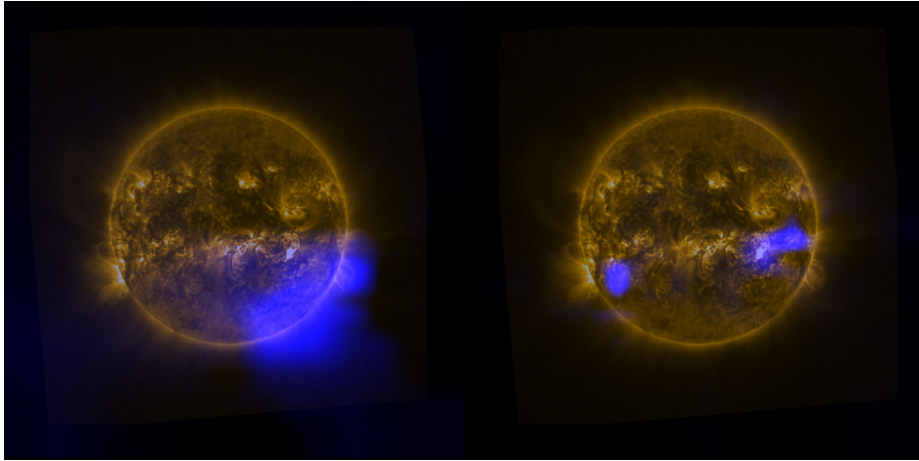
Figure 12 Two representative SWAP images of the 18 April 2014 flare observed by Carley, Vilmer, and Gallagher (2016) at 13:00 UT, with NRH data sets at 150.9 MHz (*left*) and 432.0 MHz (*right*) over-plotted (*blue*).

were combined with *Nançay Radioheliograph* (NRH: Kerdraon and Delouis, 1997) contours (between 150 and 445 MHz) to map and compare the CME front and sources of particle acceleration, which were found to be in good spatial correspondence. Figure 12 shows two representative SWAP images of the 18 April 2014 flare observed by Carley, Vilmer, and Gallagher (2016), with NRH data sets at 150.9 MHz and 432.0 MHz over-plotted.

Carley et al. (2017) reported on the observation of a Type-IV radio burst associated with a CME occurring on 01 September 2014. A combination of spectral flux-density measurements from the Nançay instruments and the *Radio Solar Telescope Network* (RSTN: Guidice, 1979) were used to reveal a gyro-synchrotron spectrum with a peak flux density at $\approx$1 GHz. Using these measurements with a gyro-synchrotron radiation model, and a non-thermal electron-density diagnostic, Carley et al. were able to calculate both the magnetic-field strength and the properties of the emitting energetic electrons within the CME. They found that the radio emission was produced by non-thermal electrons of energies >1 MeV in a CME magnetic field of 4.4×10^{-4} T at a height of 1.3 R$_\odot$. SWAP and AIA observations were used to help constrain the source of the radio emission, However, only SWAP was capable of tracking structures beyond 1.3 R$_\odot$ (see Figure 2 in Carley et al., 2017).

Bain et al. (2014) also combined NRH observations with large-FOV EUV and WL imagery to study a *moving* Type-IV radio burst (Type-IVM), which occurred in association with a CME observed on 14 August 2010. The Type-IVM source was found to be co-spatial with the CME core, which was identified in SWAP, AIA, and LASCO observations (see Figures 3 and 4 of Bain et al., 2014). Similar to Carley et al. (2017), observations with optically thin gyro-synchrotron emission were present, and compared to models they allowed the authors to estimate several key parameters of the underlying plasma: a low-energy cutoff of $10-100$ keV, with a non-thermal electron density in the range $1 \times 10^6 - 1 \times 10^8$ m^{-3}, in a magnetic field of a few 10^{-4} T. By looking at the energy-loss timescales, it was also proposed that electrons accelerated during the initiation phase may have been trapped within the CME core, removing the need for the electrons to be replenished.

Similarly, Morosan et al. (2019) also analyzed a complex Type-IV burst that accompanied a flare and CME observed on 22 September 2011. Using radio imaging from the NGH, spec-

troscopic datasets from several spectrometers (see references within), and EUV imagery (including limb-enhanced SWAP observations), Morosan et al. showed the 22 September 2011 eruptive flare was accompanied by numerous radio bursts, including a prominent Type-IV emission that changed over time. The Type-IV radio burst was found to have two components: an earlier stationary Type-IV showing gyro-synchrotron behavior, and a later moving Type-IV burst covering the same frequency band.

Tun and Vourlidas (2013) used multi-wavelength radio imaging techniques to derive the magnetic field within the core of a CME observed on 14 August 2010, where the core was found to be the source of a moving Type-IV radio burst. Tun and Vourlidas used the two viewpoints from STEREO to make stereoscopic reconstructions to constrain emission models (Thernisien, Vourlidas, and Howard, 2009) and derive the core three-dimensional trajectory, electron density, and line-of-sight depth. The authors tracked the detachment of the filament off the solar limb, out through the SWAP FOV into the LASCO FOV, overlaying 173-MHz radio contours from the NRH observations (see Figure 1 in Tun and Vourlidas, 2013). The authors found the CME to carry substantial numbers of mildly relativistic electrons ($E < 100$ keV) in a strong magnetic field, and that the spectra at lower heights were preferentially suppressed at lower frequencies due to absorption from thermal electrons.

Maguire et al. (2021) investigated a well-observed EUV jet, a WL streamer and a metric Type-II radio burst observed by the *LOw Frequency Array* (LOFAR: van Haarlem et al., 2013), on 16 October 2015. LOFAR interferometrically imaged the fundamental and harmonic sources of the Type-II radio burst and revealed that the sources did not appear to be co-spatial. By correcting for the separation Maguire et al. showed the Type-II radio sources were located ≈ 0.5 R$_\odot$ above the jet, propagating at a speed significantly faster than the jet. This suggests that the Type-II burst was generated by a piston shock driven by the jet in the low corona. SWAP observations were used to highlight locations of the fundamental and harmonic sources (see Figure 3 in Maguire et al., 2021), which originated in the middle corona, above the FOV of AIA and below the inner edge of LASCO.

In a series of articles, Frassati et al. (2017, 2019a,b) studied the early phases of a CME-driven shock, observed on 1 November 2014, through SWAP, AIA, and LASCO observations. Although the associated filament eruption occurred near the limb, it resulted in a partial-halo CME. During its early propagation, the CME produced a Type-II radio burst (seen by the *Bruny Island Radio*, BIRS: Erickson, 1997). In order to identify the source of the burst, Frassati et al. studied the kinematics of the eruption through EUV images, extrapolating out to ≈ 2 R$_\odot$. Profiles of the observed EUV front speed were compared with Alfvén speed profiles. The northern portion of the front was found to become super-Alfvénic at the same time as the start of the Type-II radio burst.

Frassati et al. (2019a) derived velocity and density maps, and a detailed investigation of the CME-driven shock associated with the event was performed. By comparing the temperature up- and down-stream of the shock with estimates of the adiabatic compression, no additional heating mechanisms were identified during the initiation phase, implying that the shock formed beyond the AIA field of view, in the middle corona.

A backside CME observed on 23 July 2012 received a lot of attention due to the energetics involved; if it had been Earth directed it is believed it would have been one of the most geoeffective events of the last century, rivaling the 1859 Carrington storm (e.g. Baker et al., 2013). The associated solar energetic particle (SEP) event had a > 10-MeV proton flux peaking at ≈ 5000 pfu, and the associated energetic-storm particle event was an order of magnitude larger. Gopalswamy et al. (2016) compared the event with other well-connected SEP events of Cycle 23, and they found a positive correlation between the CME initial speeds and the fluence spectral indices; the highest initial speeds were associated with SEP events with the hardest spectra. The 23 July event was in the group of hard-spectrum events.
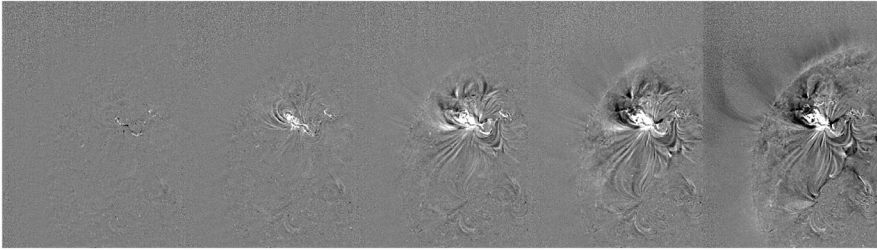
Figure 13 Five successive base-difference (preevent image subtracted) SWAP images of the EUV wave observed on 7 March 2012 by Feng et al. (2020), at ≈00:05 UT, ≈00:10 UT, ≈00:15 UT, ≈00:20 UT, and ≈00:25 UT. Each panel shows the North-East hemisphere of the Sun, extending approximately from the disk center (on the right) to 1.2 $R_\odot$. The wave is observed to propagate over the solar disk to distances > 1 $R_\odot$ from the source region.

The 23 July eruption was located behind the solar disk during its early phases, from the Earth perspective, and near the limb from the perspective of STEREO-B. Although not shown, Gopalswamy et al. used SWAP and EUVI observations to estimate the time–height profile of the eruption. Observations of associated Type-II bursts suggest the presence of a strong shock, which along with estimates of the shock speed (> 2000 km s^{-1}), the initial acceleration (≈ 1.7 km s^{-2}), and the shock-formation height (≈ 1.5 $R_\odot$), confirms that the 13 July 2012 event was likely to be an extreme event in terms of the energetic particles it accelerated.

3.2.5. EUV Waves

Most phenomena related to, or generated by, eruptions, such as flares, coronal dimmings, and EUV waves (e.g. Hudson and Webb, 1997; Thompson et al., 1998; Zhukov and Auchère, 2004; Cliver et al., 2005; Thompson and Myers, 2009), are generally observed on, or close to, the solar disk. However, EUV waves, when observed close to the solar limb can have a significant radial component in the extended EUV atmosphere. They are often, but not always, observed with eruptions, and have eruption–EUV wave association rates recorded between 58% and 95% (see references in O'Hara et al., 2019).

The nature of EUV waves is still debated; there is strong evidence that some of them might be fast magnetosonic waves, or at least have a fast magnetosonic-wave component (West et al., 2011). EUV waves are often linked to shocks leading the front and flanks of an eruption, especially when observed near the limb, which often share similar propagation angles to the waves (Biesecker et al., 2002). Several studies have used SWAP to study such waves, their kinematics, and their association with eruptions. However, these structures are not always easy to reconcile. O'Hara et al. (2019) attempted to associate EUV waves observed in the lower corona with the 1 and 3 April 2017 west-limb eruptions observed by SWAP while it was off-pointed to the West (see Section 3.2.2). The extended SWAP FOV not only provided an opportunity to track the erupting structures above the limb, but also to track the full extent of the off-limb wave, connecting the wave to the eruption front in the lower corona. The wave showed a weak correlation with the expanding eruption, although an in-depth analysis was not pursued.

Koukras et al. (2020) also utilized the off-pointed SWAP observations of 3 April 2017, along with several other instruments, a ray-tracing method, and the WKB (Wentzel–Kramers–Brillouin) approximation to analyze the kinematics of EUV waves in the inner
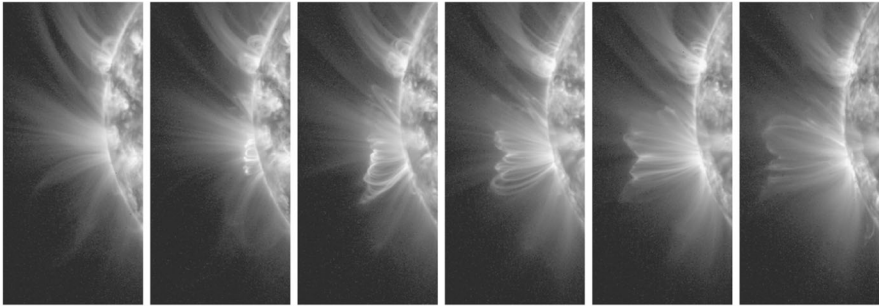
Figure 14 Successive SWAP images of the emerging posteruptive loops observed in October 2014, as reported by West and Seaton (2015), at: 20:24 UT on 14 October 2014; 01:15 UT, 10:09 UT, and 19:37 UT on 15 October 2014; and 04:10 UT and 12:48 UT on 16 October 2014. (Figure 2 from West and Seaton, 2015, used with permission).

corona, and also their connection with Type-II radio bursts. Koukras et al. were able to provide supporting evidence that EUV waves are likely fast-mode MHD waves, and further constrain the source regions of the radio-burst emission associated with the event.

Feng et al. (2020) utilized the large FOV of SWAP, with AIA and EUVI observations, to build 3D reconstructions of *EUV disturbances* (coronal-wave surfaces) observed on 7 March 2012, using a new mask-fitting method, adapted from one used to track CMEs (Feng et al., 2012). The observed disturbance and associated shock front were fitted with a three-dimensional (3D) ellipsoidal model. To detect temporal variations in the EUV observations, Feng et al. applied a running-center-median (RCM) filtering method (Plowman, 2016), allowing them to track the EUV wave to over 1.5 $R_\odot$ in both SWAP and STEREO observations (see Figure 4 in Feng et al., 2020). They observed the speed of the 3D-wave nose to increase from a value below a few hundred $\mathrm{km\,s^{-1}}$ to a maximum value around 3800 $\mathrm{km\,s^{-1}}$, before slowly decreasing afterwards. It is speculated that the low initial speed may be due to the magnetic reconfiguration in the beginning. They also found that the wave in the extended corona had a much higher speed than the speed of EUV disturbances across the solar disk. Surprisingly, Feng et al. observed poor correlation between the measured wave speeds, the flare class, and the CME speed, nor were the EUV disturbances strongly associated with Type-II radio bursts. Figure 13 shows five successive base-difference SWAP images of the EUV wave observed on 7 March 2012 by Feng et al. (2020).

Around 2011, when the STEREO spacecraft were in a quadrature configuration with Earth (positioned approximately 90° either side of the Sun–Earth line), structures could be observed simultaneously head-on and in profile. Kienreich et al. (2013) used a combination of SWAP and EUVI observations from 27 January 2011 to study three consecutive large-scale coronal waves. They were observed to emanate from near the disk center from the STEREO-A perspective, and along the limb in SWAP observations (see Figures 1 and 2 in Kienreich et al., 2013). Each wave was observed to reflect off of a southern polar coronal hole, obeying the Huygens–Fresnel principle.

The study of Kienreich et al. (2013) revealed that the velocities of the reflected waves were diminished when compared to the incident wave. However, they were proportional, indicating a continual change, rather than a loss of energy due to the interaction with the coronal hole. These results, together with an observed correlation between the speed and the strength of the waves, suggest that the EUV transients are nonlinear large-amplitude MHD waves. One surprising result observed in the SWAP off-limb observations, was that a component of the reflected wave propagated toward larger coronal heights. This study

suggests a further need to investigate coronal waves in the extended EUV atmosphere with more sensitive instrumentation, and perhaps through a hotter passband, where EUV waves are measured with a higher contrast.

3.2.6. Posteruptive Loop Systems

Another phenomenon associated with eruptive flares is posteruptive loop systems. These systems are observed to build up in the lower corona following an eruption, and they are usually interpreted as a signature of hot plasma trapped on field lines that are generated by magnetic reconnection in the posteruption current sheet (e.g. Forbes and Acton, 1996). When the eruption occurs close to the limb, these systems can be seen to grow with height as successive magnetic fields are ejected from the reconnection region. Usually, the systems are observed to stop growing after a few hours, and they terminate in the lower corona. However, on 14 October 2014, West and Seaton (2015) observed an eruption with SWAP that led to the formation of perhaps the largest posteruptive loop system seen in Solar Cycle 24. The system grew for an unprecedented 48-hour period, and to a height of approximately 4×10^5 km ($> 0.5\,R_\odot$). Figure 14 shows successive SWAP images of the emerging posteruptive loops observed in October 2014, from West and Seaton (2015). The first panel shows the preeruptive EUV structure, and the final panel shows the system after the termination of the growth phase.

Although rare, large-scale loop systems have been observed before, in particular in X-ray observations, where they were described as *postflare giant arches* (e.g. de Jager and Svestka, 1985). Originally it was concluded that these giant arches could not be generated by the same mechanism that generates classical postflare loops, because reconnection could not be sustained to such great heights. However, the model of Forbes and Lin (2000) showed that it was possible to maintain this reconnection. The observations of West and Seaton (2015) help to validate this model, and indicate that ordinary posteruptive loops and so-called postflare giant arches are fundamentally formed by the same mechanism.

3.2.7. Stealth CMEs

Stealth CMEs are a special subset of solar eruptions that do not exhibit any lower coronal signatures, e.g. waves, flares, EUV eruptive signatures, etc. (e.g. Howard and Harrison, 2013). These are of special interest to the space-weather forecasting communities as they can create space-weather events with little warning. The nature of stealth CMEs suggests a different production mechanism is at play, and/or special conditions are created by which observables are not generated. There is some evidence that stealth CMEs originate high in the solar corona, thus explaining the lack of on-disk signatures (e.g. Robbrecht, Patsourakos, and Vourlidas, 2009).

D'Huys et al. (2014) used SWAP, AIA, and LASCO to identify 40 CMEs without low-coronal EUV signatures. SWAP's large FOV helped further constrain the stealth observation set, by removing eruptions with lower and middle coronal signatures out to $1.7\,R_\odot$ along the image axes and $2.5\,R_\odot$ along the diagonal. D'Huys et al. (2014) found that stealth CMEs are diverse in appearance, often originating near the solar poles. They are generally slow events, with a limited angular width. The frequency distributions for CMEs, and separately for stealth CMEs, as a function of width, both exhibit linear behavior suggesting scale invariances (see Figure 10 in D'Huys et al., 2014), but the different power laws observed between the types of CME suggest they are governed by different eruption mechanisms. However, the kinematic profiles of stealth eruptions fit both the breakout model (e.g. Lynch et al., 2004) and models of ideal MHD instabilities (e.g. Kliem and Török, 2006).

Alzate and Morgan (2017) used the same set of 40 stealth CMEs identified from the study by D'Huys et al. (2014), but they applied the MGN image-processing technique to both the AIA and SWAP images (where possible) to search for lower coronal signatures. Alzate and Morgan (2017) identified several associated signatures, such as small flares, jets, or filament eruptions. Of the largest stealth CMEs, seven were associated with jets and a further eight with filament eruptions. In general, Alzate and Morgan were in agreement with the conclusions of D'Huys et al. (2014), in that lower coronal signatures of stealth CMEs are very faint events that either form high in the corona, or in low-density regions of magnetic field. The conclusion that such eruptions can form higher in the corona is important justification for low-noise, wide-field imagers to be used for space-weather forecasting, particularly away from the Sun–Earth line.

3.2.8. Problem Eruptions for Space-Weather Forecasting

As discussed above, solar eruptions are one of the most impressive manifestations of space weather, producing some of the most dramatic geoeffective events (e.g. Temmer, 2021). Therefore, predicting if, and when, an eruption may strike the Earth, or another body in the solar system, is of great interest to the space-weather forecasting community. In their simplest form, eruptions emerge radially from the Sun with a constant speed, or acceleration, allowing for an accurate estimate of their kinematics, and potential trajectory. However, many events deviate from this simplistic scenario.

A tricky sub-category of eruption experienced by the space-weather forecasting community are those that become *deflected* at initiation, or during transit through the heliosphere. Deflections often occur in the lower or middle corona during the acceleration phase.

Sieyra et al. (2020) used a combination of SWAP, AIA, LASCO, the SECCHI instruments, and Hα GONG observations (NSO/GONG Hα Archive: Harvey et al., 2011; Hill, 2018) to perform an extensive analysis of 13 CME events that experienced deflections from their nominal trajectory during their early development in the low corona, between October 2010 and September 2011. By using forward-modeling and tie-pointing to constrain the 3D positions of eruptions, the direction of propagation for each event could be carefully analyzed. Tie-pointing, the identification of the position of a structure from different perspectives along an intersecting plane, is the most used method for reconstructing CMEs in coronagraph data, and is closely related to triangulation, see Mierla et al. (2010) for further details. Sieyra et al. (2020) used PFSS models to estimate the coronal magnetic-field structure in the ambient corona, and the influence this had on the early phases of the eruption.

The results from Sieyra et al. (2020) highlight the need to understand the ambient magnetic environment for determining the trajectory of CMEs, both in latitude and longitude. Moreover, the variety of behaviors exhibited by different eruptions made systematization a difficult task. The large FOVs of SWAP and EUVI were instrumental in bridging the EUV-WL gap (see Section 3.2.2), allowing a more comprehensive study of the lower coronal evolution.

Cécere et al. (2020) also used the tie-pointing reconstruction technique on EUV and WL observations to characterize the 3D evolution of one of the deflected eruptions cataloged by Sieyra et al. (2020), observed on 24 January 2011. The eruption presented an interesting case study as it suffered a large deflection from its source region and expected trajectory, which amounted to 42° in latitude and 20° in longitude, before experiencing a subsequent deflection later in its propagation. The initial deflection occurred in the lower and middle corona regions, at altitudes below 4 R$_\odot$. The large FOV of SWAP was used to help characterize the early evolution of the eruption. Extrapolated magnetic fields helped confirm the presence of
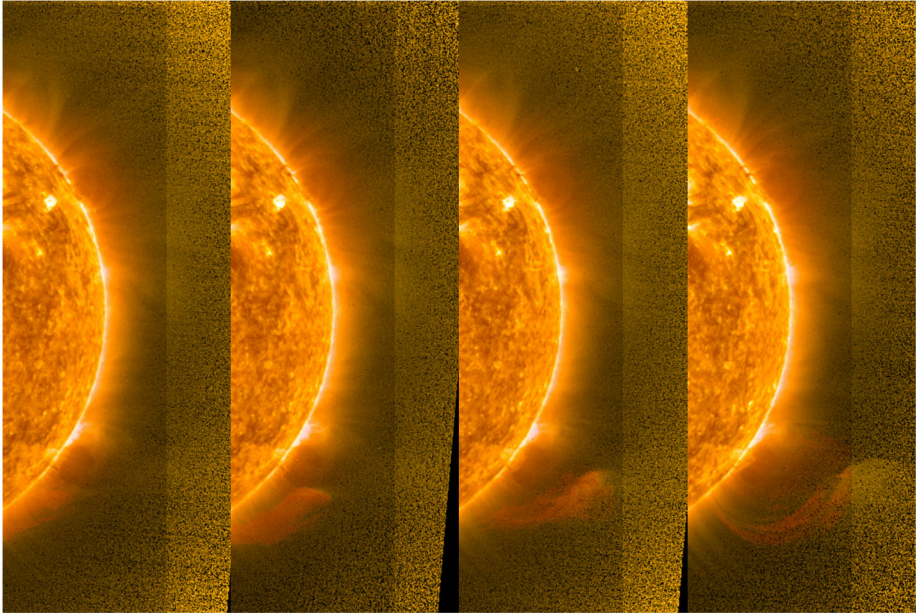
Figure 15 Successive SWAP–AIA (30.4 nm) composite images of the deflected eruption studied by Cécere et al. (2020), observed on 24 January 2011 at ≈00:00 UT, ≈01:00 UT, ≈02:00 UT, and ≈03:00 UT.

two magnetic structures near the eruption source region. Figure 15 shows successive composite SWAP images, with AIA (30.4 nm) observations overlaid, of the deflected eruption studied by Cécere et al. (2020).

The results from Cécere et al. (2020) showed that the magnetic fields associated with a southern coronal hole acted as a magnetic wall, producing a latitudinal deflection, while a nearby pseudo-streamer, and a northward extension of a coronal hole may have been responsible for an eastward deflection of the CME.

Front-sided *halo* CMEs (typically observed in WL observations), which are seen to entirely or partially encompass the solar disk, are generally of greater interest to the Earth-orientated space-weather communities, usually being associated with geomagnetic storms (e.g. Rodriguez et al., 2009). In contrast, most limb eruptions are observed to travel perpendicular to the Sun–Earth line and are not always geoeffective, or of primary interest to the space-weather community. However, some *wide* limb eruptions can also be geoeffective, but often only result in glancing encounters (less geoeffective). These have been classified as another subset of problematic eruptions (see Palmerio et al., 2019, and the references within), where their geoeffectiveness is unpredictable, mainly because the eruption and associated interplanetary shock and sheath widths, deflections, and dispersions cannot be accurately predicted.

Palmerio et al. (2019) used multi-point measurements to study the propagation of four such problematic CMEs that erupted from the solar limb (from the Earth perspective), were observed between 21 – 23 May 2013, and were detected in interplanetary space both by the STEREO-A spacecraft and in the near-Earth environment by a variety of instruments. The onset and lower coronal signatures of the eruptions were tracked using SWAP and EUVI (see Figure 2 in Palmerio et al., 2019). The propagation and possible deflection were modeled using 3D fitting with the graduated cylindrical shell (GCS) model (Thernisien, Howard,

and Vourlidas, 2006). Palmerio et al. (2019) found that predicting moderate geomagnetic disturbances, such as those generated by glancing blows, can be difficult to forecast, and they emphasized the utility of observations off of the Sun–Earth line in tracking the kinematics of problem events, especially from multiple vantage points.

A further problem for the space-weather forecasting community is represented by *failed eruptions* (e.g. Gilbert, Alexander, and Liu, 2007), where lower coronal signatures are similar to those of a regular CME, but the eruption either does not occur or initially lifts off before falling back towards the lower corona.

Tavabi, Koutchmy, and Bazin (2018) analyzed a failed plasmoid (blob) eruption using a combination of observations, including off-limb SWAP observations, and ground-based observations from the 11 July 2010 total solar eclipse. Summed SWAP images were used to improve signal-to-noise in the off-limb corona, and isophote maps produced to track the plasmoid through the SWAP FOV. These were co-aligned with WL observations allowing a complete analysis of the blob velocity (12 $\mathrm{km\,s^{-1}}$). Electron densities of the blob were photometrically evaluated, and a density of $\approx 10^{14}$ $\mathrm{m^{-3}}$ at 1.7 $\mathrm{R_\odot}$ was derived. The mass of the cloud was found to be $\approx 1.6 \times 10^{10}$ kg, which is typically 0.6×10^{-4} of the background coronal mass. The blob was seen to emerge and decelerate. It is noted that such small events could supply material for the ubiquitous slow solar wind.

Kumar and Cho (2014) used multiple instruments, including SWAP, to analyze the activation of a small filament associated with a kink instability on 30 April 2012. The eruption was initially triggered by magnetic reconnection at one of the footpoints of the filament, which subsequently underwent an unwinding motion, but failed to erupt. However, subsequent magnetic-reconnection events occurred above the kinked filament causing the flux rope to slowly rise (≈ 100 $\mathrm{km\,s^{-1}}$), producing a large twisted structure. Observations from SWAP and AIA revealed a cool compression front surrounding the expanding hot flux-rope structure.

4. SWAP-Based Studies of Coronal EUV-Emission Generation

Few studies have focused on understanding the dominant EUV-emission mechanisms in the extended corona (see Section 2.1). The first study of the coronal lines up to about 3 $\mathrm{R_\odot}$ was made by Del Zanna et al. (2018). They provided estimates of the expected quiet-Sun signal that might be observed by the proposed *EUV CME and Coronal Connectivity Observatory* (ECCCO; previously referred to as the *COronal Spectrographic Imager in the EUV* (COSIE: Golub et al., 2020)), through the 18.6–20.5 nm range, using a simple model to reproduce observed EUV radiances. However, prior to this, the only significant study of the extended corona emission was performed by Goryaev et al. (2014), who modeled an active-region streamer out to 2 $\mathrm{R_\odot}$ using SWAP observations.

To compute the EUV emission of coronal plasma in a coronal streamer structure observed in October 2010, Goryaev et al. (2014) investigated the underlying plasma properties, by performing a photometric study using the SWAP instrument during a special off-point campaign. SWAP observations were combined with *EUV Imaging Spectrometer* (EIS: Culhane et al., 2007) measurements from the *Hinode* spacecraft, as part of the international campaign for coordinated observations (HOP 165: www.isas.jaxa.jp/home/solar/hinode_op/hop.php? hop=0165). Goryaev et al. used a line-ratio method to derive the plasma density and temperature out to 1.2 $\mathrm{R_\odot}$, where the temperature in the streamer ray was found to increase smoothly from 1.25 MK at the limb to 1.35 MK at 1.2 $\mathrm{R_\odot}$. The electron density decreased from $\approx 2 \times 10^{15}$ $\mathrm{m^{-3}}$ to $\approx 3 \times 10^{14}$ $\mathrm{m^{-3}}$.

Distributions of plasma parameters higher up along the streamer ray were determined using a forward model of coronal brightness, combined with SWAP (EUV) and Mk4 coronagraph (WL) emission. Between 1.2 and 2 $R_{\odot}$ the plasma was found to be nearly isothermal ($T = 1.43 \pm 0.08$ MK), in line with earlier UVCS results. However, the density decreased to $\approx 1-2 \times 10^{13}$ m^{-3}. Using this density with a simple hydrostatic scale-height model, the temperature was estimated to be $T = 1.72 \pm 0.08$ MK, which is significantly higher than the measured value. Therefore, the density drop is slower than anticipated, indicating the streamer contains a non-thermal component of motion, perhaps associated with an outward plasma flow.

Goryaev et al. (2014) used the plasma parameters derived above and atomic data from the CHIANTI atomic database (Dere et al., 1997) to calculate emissivities in the observed spectral lines produced by collisional excitation and resonant scattering. Goryaev et al. conclude that collisional excitation contributed >90% of the observed EUV emission inside the streamer. In the background corona, the contribution to the emission from resonance scattering became comparable with that of collisions at $R \gtrsim 2\,R_{\odot}$.

Goryaev et al. further analyzed the October 2010 streamer, and flows (blobs) from the streamer, as part of a study by Goryaev, Slemzin, and Rodkin (2020), where they analyzed the relationship between the mean charge and the charge-state distributions of Fe ions. They found the expected distribution to be consistent with one produced from an equilibrium plasma with a mean temperature 1.43 MK. They also found that the *hot* ion component of streamer blobs are nearly frozen-in at 2.2 $R_{\odot}$, where the temperature equals the mean temperature of the streamer.

Goryaev et al. (2018) used SWAP observations of two large eruptive flares (X9.3 and X8.2), observed on 6 and 10 September 2017, respectively, to investigate resonant scattering of the flare radiation by the Fe IX – Fe XI ions in the coronal plasma.

The X9.3 flare was observed to increase coronal brightness up to $30-45\%$ at heights of $\approx 1.35-1.7\,R_{\odot}$. Numerical simulations indicate this might be produced by resonant scattering of the flare radiation by the Fe ions at a temperature of $T \approx 0.8-1$ MK, a density of $\approx 10^{11}$ m^{-3}, and outward velocities of $30-40$ km s^{-1}. The brightening was followed by a darkening of $30-40\%$ due to the evacuation of the coronal plasma by the associated CME.

The X8.2 flare was also accompanied by a CME, which depleted the plasma density at the observed temperatures, dimming the background corona. A DEM analysis performed with AIA measurements showed a decrease in the background plasma electron density, at distances $1.24-1.33$ $R_{\odot}$ by $2-3.5$ times after the CME, with $T \approx 1-2$ MK. At the same time, an additional DEM peak at $T \approx 0.8$ MK appeared, which Goryaev et al. (2018) concluded may be produced by flare radiation resonantly scattered by the coronal plasma.

In an article by Tavabi, Koutchmy, and Bazin (2018), which focused on the precise measurements of a failed plasmoid (blob) eruption, where SWAP's EUV photometric data were evaluated and instrumental stray-light removed, the weak 17.4-nm emission of the plasmoid was suggested to be produced by resonant scattering in the Fe IX/X lines, similar to that considered by Schrijver and McMullen (2000) to explain the background haze observed in TRACE images of the quiet corona.

5. Discussion and Conclusion

The SWAP instrument is an EUV imager observing the Sun through a spectral bandpass centered on 17.4 nm, around the Fe IX/X emission lines, corresponding to a temperature of $T \approx 0.8$ MK. Although SWAP has been observing nearly continuously for over one solar

cycle, minimal degradation has been experienced. There is on average 1% sensitivity loss per year (as measured from the built-in LED). Each year, an additional ≈2500 pixels stop working (e.g. hot pixels), resulting in about 3% of all pixels malfunctioning at the time of writing. It was originally designed as a technology demonstration, with a secondary mission goal as a tool for scientific research. A third goal was introduced later in the mission's life: to monitor space weather (see Section 5.1) for the ESA Space Safety Program (S2P) Space WEather (SWE) segment.

The longevity of the SWAP mission has allowed investigations into the long-term evolution of the extended EUV corona (see Section 3.1.4). Mierla et al. (2020) and Seaton et al. (2013a) showed the evolution of the extended EUV corona to have a strong solar-cycle dependence, correlating with solar activity recorded through sunspot numbers.

SWAP was designed to include many innovations; however, its most prominent feature has been its extended FOV, which has provided access to the off-limb EUV corona out to 1.7 $R_\odot$. The lack of observations at these heights has been driven by historical decisions to prioritize observations of the inner corona. Optimization choices have led to the extended coronal signature being compressed in some cases, such as that experienced by EUVI (e.g. Howard et al., 2008), and an understanding that EUV emission in the middle corona is too weak to observe with current instrumentation (e.g. Schrijver and McMullen, 2000).

As discussed in Section 2.1, the difference in emission generated between the hot, dense plasma found in the lower corona, and the rarefied plasmas observed in the middle corona can lead to large disparities in the dynamic range (which can exceed 10^5). To enhance the signal in the middle coronal regions, instruments have to collect more photons, either by increasing the aperture size of the instrument, or by increasing the exposure time. However, this can lead to saturation in the bright regions observed on the solar disk. As such, instruments have often focused on lower coronal structures, and relied on post-processing techniques, such as those described in Section 2.2, to enhance extended corona observations.

Although the SWAP instrument uses post-processing to generate its Carrington data sets, it has occasionally performed campaigns with longer exposures. SWAP has a CMOS detector, which has the advantage over typical charge-coupled devices (CCDs) in that it does not experience blooming effects when pixels become saturated. Blooming can lead to loss of information not just in the saturated pixel but also in surrounding pixels. The SUVI instrument, the large-FOV imager on the GOES-R platforms, has incorporated antiblooming circuitry in its CCD to avoid blooming-saturated pixels (Darnel et al., 2022), allowing SUVI to observe extremely bright features, such as solar flares, without the destructive image effects of blooming.

The next generation of instruments that is being designed to observe the extended EUV corona will also incorporate novel techniques to compensate for the dynamic-range disparity. The COSIE instrument (Golub et al., 2020) will use a spot filter over the brightest part of the Sun and then stack multiple images to increase the photon count in the outer FOV, without saturating the inner FOV. Alternatively, the *Sun Coronal Ejection Tracker Concept* (SunCET: Mason et al., 2022) mission will leverage new CMOS-APS detector technology to read out different areas of the detector with different integration times, resulting in a simultaneous high dynamic range.

The misapprehension that EUV emission in the middle corona is too weak to observe with current instrumentation is discussed by Seaton et al. (2021), but it stems from a lack of direct measurements of the region. It is discussed by Del Zanna et al. (2018) that the EUV intensity of the solar disk is comparable with that of the inner corona observed off-limb, but the behavior of the coronal lines up to about 3 $R_\odot$ was not known until their study. There were no direct measurements of coronal lines up to 3 $R_\odot$ in the quiet Sun, and the only study

of the extended EUV corona is that by Goryaev et al. (2014), who concluded that collisional excitation contributed >90% of the observed EUV emission inside the streamer. However, in the background corona, the contribution to the emission from resonance scattering became comparable with that of collisions at $R \gtrsim 2$ R$_\odot$. The lack of measurements can be directly attributed to the difficulties in observing the region, and the nearly exponential decay of the electron density with radial distance (see Section 2.1).

SWAP EUV images clearly show the complex and dynamical behavior of open and closed structures extending out into the extended EUV corona. These observations, and later those from SUVI and EUI FSI, have increased interest in the region, particularly the middle corona, the region spanning heliocentric altitudes 1.5 and 6 R$_\odot$. The region is believed to encompass almost all of the influential physical transitions and processes that govern the behavior of coronal outflow. Importantly, it also modulates inflow from above that can drive dynamic changes at low heights (e.g. Seaton et al., 2021). Correspondingly, this region is essential for understanding and developing global models of the corona, the heliosphere, and the eruptions that propagate through them.

As discussed in Section 3.2 the initiation phase of an eruption often occurs at heights < 2 R$_\odot$, and the impulsive acceleration phase mainly occurs below, or within the middle corona. As a consequence, the extended FOV of SWAP has been utilized by several authors (e.g. Fainshtein and Egorov, 2013; Mierla et al., 2013; Sarkar et al., 2019) to study eruptions through these early stages, which are crucial in shaping the kinematics of the eruptions.

Although SWAP has the largest FOV of any EUV imager along the Sun–Earth line, an observational gap (Byrne et al., 2014; D'Huys et al., 2017; Reva et al., 2017) still exists between its outer edge and the inner edge of WL LASCO (the only space-based coronagraph also observing along the Sun–Earth line). Several studies have tried to bridge this gap (see Section 3.2.2), either by using off-pointed SWAP observations (e.g. O'Hara et al., 2019) to bring the EUV observations to the inner edge of the WL observations, or alternatively by using ground-based coronagraphs with lower FOVs (e.g. Mk4; see Byrne et al., 2014), or complementary eclipse observations (e.g. Pasachoff et al., 2011, 2015; Bazin, Koutchmy, and Tavabi, 2013), although these observations are intermittent and cannot be used on a continuous basis. The observational gap is gradually being filled with new EUV and WL instruments.

SUVI has been making periodic off-point observations of the extended EUV atmosphere since 2019 (Darnel et al., 2022). Seaton et al. (2021) used SUVI to carry out the first comprehensive study of the dynamics of the extended EUV atmosphere through multiple bandpasses on long timescales. The EUI FSI instrument onboard Solar Orbiter, launched in 2020, thanks to its unique orbit, has made the widest observations of the EUV atmosphere through its 17.4-nm passband, which extend out to several R$_\odot$. For comparison, Figure 16 shows a SWAP and an EUI image (from SolO/EUI Data Release 5.0: Mampaey et al., 2022) side by side, when EUI was positioned at a heliocentric distance of 0.4 Astronomical Units (AU); the blue square in the left image highlights the periphery of the SWAP FOV.

The next generation of EUV instruments is being designed specifically to capture the extended EUV corona, into the middle corona. SunCET is a new mission being developed and designed to observe through a bandpass around 19.5 nm, out to 4 R$_\odot$ (Mason et al., 2021). Separately, COSIE is a coronal spectrograph and imager (Golub et al., 2020), which will observe out to around 3 R$_\odot$, and is currently being proposed to capture the energetics of eruptions in their infancy.

From the WL perspective, the *Association of Spacecraft for Polarimetric and Imaging Investigation of the Corona of the Sun* (ASPIICS: see references within Shestov et al., 2021) is a novel externally occulted solar coronagraph currently scheduled to be launched in 2023
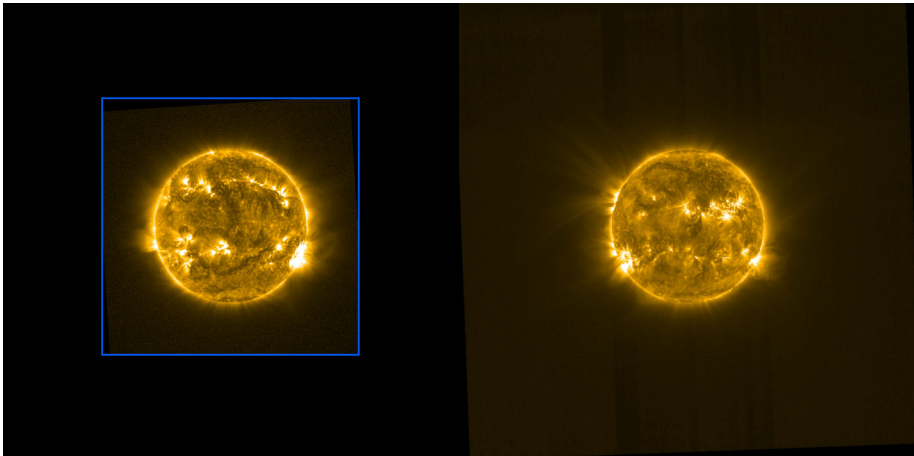
Figure 16   SWAP (*left*) and EUI FSI (*right*) images from 08 April 2022 at 22:20 UT, when EUI had a separation angle of 132° with respect to the Sun–Earth line, near the back of the Sun, and at a heliocentric distance of 0.4 AU. The *blue square in the left image* highlights the periphery of the SWAP FOV.

onboard the PROBA3 platform. The external occulter will be placed on a separate satellite allowing WL observations between ≈ 1.1 R$_\odot$ and 3.0 R$_\odot$. Similar FOVs are also being proposed on the *Visible Emission Line Coronagraph* (VELC) coronagraph to be launched onboard the *Aditya-L1* mission (Seetha and Megala, 2017).

Due to the observational gap few studies have been able to track eruptions directly from the inner corona into the outer corona. The off-pointed SWAP observations presented by O'Hara et al. (2019) (see Section 3.2.2) were used to track an eruption directly from EUV into WL observations, allowing for a study of the eruption kinematics during the crucial acceleration phase. However, it is discussed that associating features observed through EUV passbands with those in the WL is challenging. In particular, the leading edge of the WL eruption was not found to correspond to that observed in the EUV. O'Hara et al. (2019) discuss that SWAP's temperature response peaks at around 0.85 MK (as shown in Figure 4 of Raftery et al. (2013)), and as such, the leading edge observed in the EUV observations most probably corresponds to the core of the eruption in the WL observations, rather than the leading edge, which contains cooler filament material.

For meaningful studies to be made with combined EUV and WL datasets, overlapping rather than side-by-side observations are required. Such observations would allow the observer to understand which parts of the observed structure are co-spatial. Another benefit of such observations would be to obtain thermal characteristics using the EUV bandpasses with DEM techniques (Plowman, Kankelborg, and Martens, 2013), while estimating the density from the corresponding WL observations.

The extensive use of SWAP to study solar eruptions, and its ability to monitor the sources of space-weather activity in the lower corona, have made it an invaluable tool also for space-weather forecasting, as described in the following section.

5.1. SWAP and Space-Weather Monitoring

Space weather comes in many forms, from the background solar-wind plasma, to more short-lived events, including CMEs, solar flares, and SEPs accelerated by CME-driven

shocks and flares. Even with its modest resolution, SWAP is able to observe all on-disk space-weather-related phenomena, such as flares, coronal holes, active regions, and coronal arcades (see discussion by West et al., 2020). Due to its large FOV it can also monitor off-limb structures such as the kinematics of eruptions (see Section 3.2.1), helping to improve forecasts of eruption arrival times; the positions of streamers and pseudo-streamers (see Section 3.1.1); and the position of corona holes. Each event can influence the Earth in different ways; SEPs can trigger solar-radiation storms throughout the solar system (Laurenza et al., 2009), whereas the plasmas in eruptions and the solar wind can induce geomagnetic storms and ionospheric disturbances, among other effects (see Hapgood, 2017). Due to the impacts, especially on ever-increasing space-based sensitive equipment, space-weather forecasting has become increasingly important.

The PROBA2 spacecraft has served as one of ESA's primary space-weather monitors since the start of ESA's Space Situational Awareness (SSA) programme (Luntama, Glover, and Kraft, 2018). SWAP images are used routinely in space-weather forecasts, and support several monitoring tools in the SSA Space Weather Coordination Centre (SSCC), and Solar Weather Expert Service Centre. SWAP has also supported several ESA missions through critical operational phases (Kruglanski et al., 2017).

In January 2014 the SSCC assisted the *Gaia* team (Prusti et al., 2016) during their launch window and L2 insertion manoeuvre with dedicated space-weather forecasts, and particle-storm / flaring-activity alerts. SWAP observations were used to monitor solar activity throughout the period. Similar forecasts and alerts were issued for a *Vega* rocket launch in 2015.

During the aero-braking campaign when *Venus Express* (Titov et al., 2006) entered the atmosphere of Venus (May to July 2014), SWAP was used to help monitor sources of enhanced solar radiation that could affect the atmospheric density at aero-braking altitudes.

Support was given throughout the *Rosetta* mission (Glassmeier et al., 2007), especially in September 2014 during the landing and operations of the *Philae* probe, and again in November 2014 when the spacecraft was escorting comet 67P/Churyumov-Gerasimenko around the Sun, during a critical phase of the mission.

For Mars-based missions, such as *Mars Express* (Chicarro, Martin, and Trautner, 2004), dedicated dashboards have been developed. These include annotated SWAP observations, which are used as a reference for solar activity that may produce space-weather activity affecting spacecraft operations and communication. More recently, SWAP has supported the SSCC in their forecasts for the *BepiColombo* mission (Benkhoff et al., 2021) during its Venus flybys in 2020.

5.1.1. Automatically Detecting Eruptions

Several algorithms have been constructed to automatically track and characterize eruption kinematics in WL observations, including the *Computer Aided CME Tracking System* (CAC-Tus: Robbrecht, Patsourakos, and Vourlidas, 2009) and *Solar Eruptive Events Detection System* (SEEDS: Olmedo et al., 2008). Such tools are important for the space-weather forecasting and scientific communities, who can rely on them both to provide automated warnings, and also to build up catalogs of eruption statistics.

In recent years, with processing enhancements improving the observation of off-limb EUV signals in large-FOV EUV instrumentation, instruments such as SWAP have been able to detect eruptions to greater heights in the extended EUV corona. Therefore, automated-detection algorithms could in principle be developed to supply additional, and earlier forecasts of eruptions, as well as offer a backup to WL-based techniques.

Inspired by the WL automated-detection algorithms of CACTus and SEEDS, Patel et al. (2021) used the large FOV of SWAP, along with EUVI and AIA observations to build and test an automated-tracking algorithm, *CME Identification in Inner Solar Corona* (CIISCO), that uses Fourier motion filtering and the parabolic Hough transform for the first time to automatically detect off-disk solar eruptions in the lower and middle corona. The Hough transform is suited to tracking the kinematic profiles of eruptions in their initiation and impulsive phases.

The potential for large-FOV EUV imagers to not only monitor the sources of space-weather activity in the lower corona but also eruptions off the solar limb have led to such instruments being proposed for future space-weather monitoring platforms, such as the proposed *Lagrange eUv Coronal Imager* instrument (LUCI: West et al., 2020) onboard the ESA *Vigil* (formerly *Lagrange*) mission, which would observe from the L_5 Lagrangian point.

5.2. SWAP's Legacy

In recent years there has been a push to prioritize missions that observe and connect the corona and heliosphere, in particular through observations of the middle corona. The region encompasses almost all of the influential physical transitions and processes that govern the behavior of coronal outflow, where the magnetic-field topology changes from predominantly closed to open, and the plasma β from low to high values. Historically, this region has been difficult to observe because it is too close to the Sun for practical WL observations, while EUV emission in this region was believed to be too weak to observe. Interest in this region is due in no small part to the observations from SWAP, especially the Carrington data products, which have revealed structures out through the extended EUV corona.

SWAP was able to create such an impact due to its innovative design and longevity. Its large FOV ($54' \times 54'$) combined with optional off-points, observing through a spectral bandpass centered on 17.4 nm, allowed it to monitor all space-weather related phenomena in the lower and extended EUV corona, facilitating short-term and long-term studies alike.

The low-power and compact design of SWAP led to several design choices that directly influenced the development of the EUI instrument onboard *Solar Orbiter*, and those being implemented in the LUCI instrument on the proposed ESA Vigil mission. Instruments such as the SUVI, can claim observational heritage from SWAP, in particular, the adoption of optional off-point strategies to see further into the extended EUV corona.

SWAP has revealed the large-scale structures that populate the extended corona, in particular the middle corona. The next generation of instruments being designed, or recently launched (including *SunCET*, COSIE, EUI, ASPIICS, VELC, and the *Polarimeter to UNify the Corona and Heliosphere* (PUNCH: DeForest et al., 2022)), will explore: the substructure, the underlying composition, and the energetics and dynamics that generate emission of the region. This will be performed co-spatially, at higher resolution, and through multiple passbands, providing further access to this under-explored region.

Appendix

Here, we calculate the time taken for a hypothetical point source, located at a height H from the solar-disk center, to rotate with the Sun a *projected* distance Δx from an arbitrary projected distance x_0. The corresponding angular distance is $\Delta\theta$, and the starting angle θ_0, as summarized in Figure 17a. The projected starting distance, from the disk center, can be expressed as

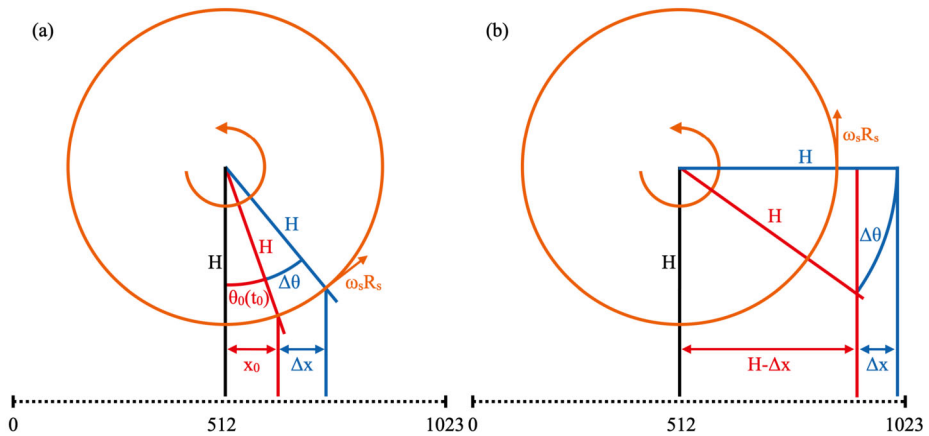$$x_0 = H \sin(\theta_0). \tag{1}$$

Figure 17 Two schematics of the Sun observed from above the equatorial plane, showing the perceived motion of hypothetical point sources, rotating with the Sun, at height H from the Sun center. Panel **a** shows a point source rotating across the solar disk, whereas Panel **b** shows a point source rotating off-limb, close to the plane of the sky. See text for further details.

After a period Δt, the projected distance will have changed by

$$x_0 + \Delta x = H \sin(\theta_0 + \Delta\theta). \tag{2}$$

Assuming the Sun has a constant angular rotation rate of $\omega_s = \frac{\Delta\theta}{\Delta t}$, Equation 2 can be expressed as

$$\frac{x_0}{H} + \frac{\Delta x}{H} = \sin(\theta_0 + \omega_s \Delta t), \tag{3}$$

rearranging and substituting x_0 from Equation 1 we obtain:

$$\sin^{-1}\left(\sin(\theta_0) + \frac{\Delta x}{H}\right) = \theta_0 + \omega_s \Delta t. \tag{4}$$

Rearranging for Δt, we find:

$$\Delta t = \frac{1}{\omega_s}\left(\sin^{-1}\left(\sin(\theta_0) + \frac{\Delta x}{H}\right) - \theta_0\right). \tag{5}$$

A similar derivation can be made to show the time taken for a source to rotate a projected distance to the left of the disk center:

$$\Delta t = \frac{1}{\omega_s}\left(\sin^{-1}\left(\sin(\theta_0) - \frac{\Delta x}{H}\right) + \theta_0\right). \tag{6}$$

When tracking a structure on the solar disk, we can assume $H = R_\odot$, and the point of interest rotates across the solar disk. However, close to the limb the above formalism breaks down, and equations 5 and 6 are only valid between $-1 \leq \left(\sin(\theta_0) + \frac{\Delta x}{H}\right) \leq 1$ and $-1 \leq \left(\sin(\theta_0) - \frac{\Delta x}{H}\right) \leq 1$, respectively. At the solar limb we are only interested in the time taken for a point to rotate a projected distance (Δx) close to the plane of the sky. Therefore, a simpler, less arbitrary solution is used, as outlined in Figure 17b, where the projected

distance changes from $H - \Delta x$ to H in a time Δt. The angle subtended in this period can be shown to be

$$\Delta\theta = \cos^{-1}\left(\frac{H - \Delta x}{H}\right), \tag{7}$$

where once again we can substitute for the rotation rate:

$$\Delta t = \frac{1}{\omega_s}\cos^{-1}\left(\frac{H - \Delta x}{H}\right). \tag{8}$$

Equation 8 allows for more accurate estimates of the rotation time close to the limb, over Equation 6.

Declarations

Disclosure of Potential Conflicts of Interest The authors declare that they have no conflicts of interest.

Competing interests The authors declare no competing interests.

References

Alzate, N., Morgan, H.: 2016, Jets, coronal "puffs," and a slow coronal mass ejection caused by an opposite-polarity region within an active region footpoint. *Astrophys. J.* **823**, 129. DOI. ADS.

Alzate, N., Morgan, H.: 2017, Identification of low coronal sources of "stealth" coronal mass ejections using new image processing techniques. *Astrophys. J.* **840**, 103. DOI. ADS.

Attie, R., Innes, D.E., Potts, H.E.: 2009, Evidence of photospheric vortex flows at supergranular junctions observed by FG/SOT (Hinode). *Astron. Astrophys.* **493**, L13. DOI. ADS.

Bain, H.M., Krucker, S., Saint-Hilaire, P., Raftery, C.L.: 2014, Radio imaging of a type IVM radio burst on the 14th of August 2010. *Astrophys. J.* **782**, 43. DOI. ADS.

Baker, D.N., Li, X., Pulkkinen, A., Ngwira, C.M., Mays, M.L., Galvin, A.B., Simunac, K.D.C.: 2013, A major solar eruptive event in July 2012: defining extreme space weather scenarios. *Space Weather* **11**, 585. DOI. ADS.

Bazin, C., Koutchmy, S., Tavabi, E.: 2013, Prominence cavity regions observed using SWAP 174 Å filtergrams and simultaneous eclipse flash spectra. *Solar Phys.* **286**, 255. DOI. ADS.

Benkhoff, J., Murakami, G., Baumjohann, W., Besse, S., Bunce, E., Casale, M., Cremosese, G., Glassmeier, K.-H., Hayakawa, H., Heyner, D., Hiesinger, H., Huovelin, J., Hussmann, H., Iafolla, V., Iess, L., Kasaba, Y., Kobayashi, M., Milillo, A., Mitrofanov, I.G., Montagnon, E., Novara, M., Orsini, S., Quemerais, E., Reininghaus, U., Saito, Y., Santoli, F., Stramaccioni, D., Sutherland, O., Thomas, N., Yoshikawa, I., Zender, J.: 2021, BepiColombo - mission overview and science goals. *Space Sci. Rev.* **217**, 90. DOI. ADS.

Berger, T.E., Shine, R.A., Slater, G.L., Tarbell, T.D., Title, A.M., Okamoto, T.J., Ichimoto, K., Katsukawa, Y., Suematsu, Y., Tsuneta, S., Lites, B.W., Shimizu, T.: 2008, Hinode SOT observations of solar quiescent prominence dynamics. *Astrophys. J. Lett.* **676**, L89. DOI. ADS.

Bethge, C., Peter, H., Kentischer, T.J., Halbgewachs, C., Elmore, D.F., Beck, C.: 2011, The chromospheric telescope. *Astron. Astrophys.* **534**, A105. DOI. ADS.

Biesecker, D.A., Myers, D.C., Thompson, B.J., Hammer, D.M., Vourlidas, A.: 2002, Solar phenomena associated with "EIT waves". *Astrophys. J.* **569**, 1009. DOI. ADS.

Bougeret, J.-L., Kaiser, M.L., Kellogg, P.J., Manning, R., Goetz, K., Monson, S.J., Monge, N., Friel, L., Meetre, C.A., Perche, C., Sitruk, L., Hoang, S.: 1995, Waves: the radio and plasma wave investigation on the wind spacecraft. *Space Sci. Rev.* **71**, 231. DOI. ADS.

Brueckner, G.E., Howard, R.A., Koomen, M.J., Korendyke, C.M., Michels, D.J., Moses, J.D., Socker, D.G., Dere, K.P., Lamy, P.L., Llebaria, A., Bout, M.V., Schwenn, R., Simnett, G.M., Bedford, D.K., Eyles, C.J.: 1995, The Large Angle Spectroscopic Coronagraph (LASCO). *Solar Phys.* **162**, 357. DOI. ADS.

Byrne, J.P., Morgan, H., Seaton, D.B., Bain, H.M., Habbal, S.R.: 2014, Bridging EUV and white-light observations to inspect the initiation phase of a "two-stage" solar eruptive event. *Solar Phys.* **289**, 4545. DOI. ADS.

Cargill, P.J., Chen, J., Spicer, D.S., Zalesak, S.T.: 1996, Magnetohydrodynamic simulations of the motion of magnetic flux tubes through a magnetized plasma. *J. Geophys. Res.* **101**, 4855. DOI. ADS.

Carley, E.P., Vilmer, N., Gallagher, P.T.: 2016, Radio diagnostics of electron acceleration sites during the eruption of a flux rope in the solar corona. *Astrophys. J.* **833**, 87. DOI. ADS.

Carley, E.P., Vilmer, N., Simões, P.J.A., ÓFearraigh, B.: 2017, Estimation of a coronal mass ejection magnetic field strength using radio observations of gyrosynchrotron radiation. *Astron. Astrophys.* **608**, A137. DOI. ADS.

Cécere, M., Sieyra, M.V., Cremades, H., Mierla, M., Sahade, A., Stenborg, G., Costa, A., West, M.J., D'Huys, E.: 2020, Large non-radial propagation of a coronal mass ejection on 2011 January 24. *Adv. Space Res.* **65**, 1654. DOI. ADS.

Chicarro, A., Martin, P., Trautner, R.: 2004, The Mars express mission: an overview. In: Wilson, A., Chicarro, A. (eds.) *Mars Express: the Scientific Payload*, ESA Special Publication **1240**, 3. ADS.

Cliver, E.W., Laurenza, M., Storini, M., Thompson, B.J.: 2005, On the origins of solar EIT waves. *Astrophys. J.* **631**, 604. DOI. ADS.

Culhane, J.L., Harra, L.K., James, A.M., Al-Janabi, K., Bradley, L.J., Chaudry, R.A., Rees, K., Tandy, J.A., Thomas, P., Whillock, M.C.R., Winter, B., Doschek, G.A., Korendyke, C.M., Brown, C.M., Myers, S., Mariska, J., Seely, J., Lang, J., Kent, B.J., Shaughnessy, B.M., Young, P.R., Simnett, G.M., Castelli, C.M., Mahmoud, S., Mapson-Menard, H., Probyn, B.J., Thomas, R.J., Davila, J., Dere, K., Windt, D., Shea, J., Hagood, R., Moye, R., Hara, H., Watanabe, T., Matsuzaki, K., Kosugi, T., Hansteen, V., Wikstol, Ø.: 2007, The EUV imaging spectrometer for Hinode. *Solar Phys.* **243**, 19. DOI. ADS.

Darnel, J.M., Seaton, D.B., Bethge, C., Rachmeler, L., Jarvis, A., Hill, S.M., Peck, C.L., Hughes, J.M., Shapiro, J., Riley, A., Vasudevan, G., Shing, L., Koener, G., Edwards, C., Mathur, D., Timothy, S.: 2022, The GOES-R solar UltraViolet imager. *Space Weather* **20**, e03044. DOI. ADS.

de Jager, C., Svestka, Z.: 1985, 21 May 1980 flare review. *Solar Phys.* **100**, 435. DOI. ADS.

DeForest, C., Killough, R., Gibson, S., Henry, A., Case, T., Beasley, M., Laurent, G., Colaninno, R., Waltham, N.: 2022, Polarimeter to UNify the Corona and Heliosphere (PUNCH): Science, Status, and Path to Flight. In: *2022 IEEE Aerospace Conference (AERO)*, 1. DOI.

Del Zanna, G., Raymond, J., Andretta, V., Telloni, D., Golub, L.: 2018, Predicting the COSIE-C signal from the outer corona up to 3 solar radii. *Astrophys. J.* **865**, 132. DOI. ADS.

Delaboudinière, J.-P., Artzner, G.E., Brunaud, J., Gabriel, A.H., Hochedez, J.F., Millier, F., Song, X.Y., Au, B., Dere, K.P., Howard, R.A., Kreplin, R., Michels, D.J., Moses, J.D., Defise, J.M., Jamar, C., Rochus, P., Chauvineau, J.P., Marioge, J.P., Catura, R.C., Lemen, J.R., Shing, L., Stern, R.A., Gurman, J.B., Neupert, W.M., Maucherat, A., Clette, F., Cugnon, P., van Dessel, E.L.: 1995, EIT: extreme-ultraviolet imaging telescope for the SOHO mission. *Solar Phys.* **162**, 291. DOI. ADS.

Dere, K.P., Landi, E., Mason, H.E., Monsignori Fossi, B.C., Young, P.R.: 1997, CHIANTI - an atomic database for emission lines. *Astron. Astrophys. Suppl.* **125**, 149. DOI. ADS.

D'Huys, E., Seaton, D.B., Poedts, S., Berghmans, D.: 2014, Observational characteristics of coronal mass ejections without low-coronal signatures. *Astrophys. J.* **795**, 49. DOI. ADS.

D'Huys, E., Seaton, D.B., De Groof, A., Berghmans, D., Poedts, S.: 2017, Solar signatures and eruption mechanism of the August 14, 2010 coronal mass ejection (CME). *J. Space Weather Space Clim.* **7**, A7. DOI. ADS.

Domingo, V., Fleck, B., Poland, A.I.: 1995, The SOHO mission: an overview. *Solar Phys.* **162**, 1. DOI. ADS.

Egorov, Y.I., Fainshtein, V.G.: 2013, Study of CME properties using high resolution data. *Cent. Eur. Astrophys. Bull.* **37**, 619. ADS.

Elmore, D.F., Burkepile, J.T., Darnell, J.A., Lecinski, A.R., Stanger, A.L.: 2003, Calibration of a ground-based solar coronal polarimeter. In: Fineschi, S. (ed.) *Polarimetry in Astronomy*, *Society of Photo-Optical Instrumentation Engineers (SPIE) Conference Series* **4843**, 66. DOI. ADS.

Erickson, W.C.: 1997, The bruny island radio spectrometer. *Publ. Astron. Soc. Aust.* **14**, 278. DOI. ADS.

Eyles, C.J., Harrison, R.A., Davis, C.J., Waltham, N.R., Shaughnessy, B.M., Mapson-Menard, H.C.A., Bewsher, D., Crothers, S.R., Davies, J.A., Simnett, G.M., Howard, R.A., Moses, J.D., Newmark, J.S., Socker, D.G., Halain, J.-P., Defise, J.-M., Mazy, E., Rochus, P.: 2009, The heliospheric imagers onboard the STEREO mission. *Solar Phys.* **254**, 387. DOI. ADS.

Fainshtein, V.G., Egorov, Y.I.: 2013, Investigation of CME properties using the data of SDO and PROBA2 spacecraft. *Cosm. Res.* **51**, 1. DOI. ADS.

Fainshtein, V.G., Egorov, Y.I.: 2015, Initiation of CMEs associated with filament eruption, and the nature of CME related shocks. *Adv. Space Res.* **55**, 798. DOI. ADS.

Feng, L., Inhester, B., Wei, Y., Gan, W.Q., Zhang, T.L., Wang, M.Y.: 2012, Morphological evolution of a three-dimensional coronal mass ejection cloud reconstructed from three viewpoints. *Astrophys. J.* **751**, 18. DOI. ADS.

Feng, L., Lu, L., Inhester, B., Plowman, J., Ying, B., Mierla, M., West, M.J., Gan, W.: 2020, Three-dimensional reconstructions of coronal wave surfaces using a new mask-fitting method. *Solar Phys.* **295**, 141. DOI. ADS.

Filippov, B., Koutchmy, S., Tavabi, E.: 2013, Formation of a white-light jet within a quadrupolar magnetic configuration. *Solar Phys.* **286**, 143. DOI. ADS.

Forbes, T.G., Acton, L.W.: 1996, Reconnection and field line shrinkage in solar flares. *Astrophys. J.* **459**, 330. DOI. ADS.

Forbes, T.G., Lin, J.: 2000, What can we learn about reconnection from coronal mass ejections? *J. Atmos. Solar-Terr. Phys.* **62**, 1499. DOI. ADS.

Frassati, F., Susino, R., Mancuso, S., Bemporad, A.: 2017, Study of the early phase of a coronal mass ejection driven shock in EUV images. *Astrophys. Space Sci.* **362**, 194. DOI. ADS.

Frassati, F., Susino, R., Mancuso, S., Bemporad, A.: 2019a, Comprehensive analysis of the formation of a shock wave associated with a coronal mass ejection. *Astrophys. J.* **871**, 212. DOI. ADS.

Frassati, F., Susino, R., Mancuso, S., Bemporad, A.: 2019b, Kinematics of a compression front associated with a coronal mass ejection. *Nuovo Cimento C Geophys. Space Phys.* **42**, 35. DOI. ADS.

Gibson, S.E., Fan, Y.: 2006, Coronal prominence structure and dynamics: a magnetic flux rope interpretation. *J. Geophys. Res.* **111**, A12103. DOI. ADS.

Gibson, S.E., Kucera, T.A., Rastawicki, D., Dove, J., de Toma, G., Hao, J., Hill, S., Hudson, H.S., Marqué, C., McIntosh, P.S., Rachmeler, L., Reeves, K.K., Schmieder, B., Schmit, D.J., Seaton, D.B., Sterling, A.C., Tripathi, D., Williams, D.R., Zhang, M.: 2010, Three-dimensional morphology of a coronal prominence cavity. *Astrophys. J.* **724**, 1133. DOI. ADS.

Gilbert, H.R., Alexander, D., Liu, R.: 2007, Filament kinking and its implications for eruption and re-formation. *Solar Phys.* **245**, 287. DOI. ADS.

Glassmeier, K.-H., Boehnhardt, H., Koschny, D., Kührt, E., Richter, I.: 2007, The Rosetta mission: flying towards the origin of the solar system. *Space Sci. Rev.* **128**, 1. DOI. ADS.

Golub, L., Cheimets, P., DeLuca, E.E., Madsen, C.A., Reeves, K.K., Samra, J., Savage, S., Winebarger, A., Bruccoleri, A.R.: 2020, EUV imaging and spectroscopy for improved space weather forecasting. *J. Space Weather Space Clim.* **10**, 37. DOI. ADS.

Gopalswamy, N., Yashiro, S., Thakur, N., Mäkelä, P., Xie, H., Akiyama, S.: 2016, The 2012 July 23 backside eruption: an extreme energetic particle event? *Astrophys. J.* **833**, 216. DOI. ADS.

Goryaev, F.F., Slemzin, V., Rodkin, D.: 2020, Identification of hot plasma anomalies in solar wind using fe ion charge distributions. *Astrophys. J. Lett.* **905**, L17. DOI. ADS.

Goryaev, F., Slemzin, V., Vainshtein, L., Williams, D.R.: 2014, Study of extreme-ultraviolet emission and properties of a coronal streamer from PROBA2/SWAP, Hinode/EIS and Mauna Loa Mk4 observations. *Astrophys. J.* **781**, 100. DOI. ADS.

Goryaev, F.F., Slemzin, V.A., Rodkin, D.G., D'Huys, E., Podladchikova, O., West, M.J.: 2018, Brightening and darkening of the extended solar corona during the superflares of September 2017. *Astrophys. J. Lett.* **856**, L38. DOI. ADS.

Guennou, C., Rachmeler, L., Seaton, D., Auchère, F.: 2016, Lifecycle of a large-scale polar coronal pseudostreamer/cavity system. *Front. Astron. Space Sci.* **3**, 14. DOI. ADS.

Guidice, D.A.: 1979, Sagamore Hill Radio Observatory, Air Force Geophysics Laboratory, Hanscom Air Force Base, Massachusetts 01731. Report. In: *Bulletin of the American Astronomical Society* **11**, 311. ADS.

Halain, J.-P., Berghmans, D., Seaton, D.B., Nicula, B., De Groof, A., Mierla, M., Mazzoli, A., Defise, J.-M., Rochus, P.: 2013, The SWAP EUV imaging telescope. Part II: in-flight performance and calibration. *Solar Phys.* **286**, 67. DOI. ADS.

Handy, B.N., Acton, L.W., Kankelborg, C.C., Wolfson, C.J., Akin, D.J., Bruner, M.E., Caravalho, R., Catura, R.C., Chevalier, R., Duncan, D.W., Edwards, C.G., Feinstein, C.N., Freeland, S.L., Friedlaender, F.M., Hoffmann, C.H., Hurlburt, N.E., Jurcevich, B.K., Katz, N.L., Kelly, G.A., Lemen, J.R., Levay, M., Lindgren, R.W., Mathur, D.P., Meyer, S.B., Morrison, S.J., Morrison, M.D., Nightingale, R.W., Pope, T.P., Rehse, R.A., Schrijver, C.J., Shine, R.A., Shing, L., Strong, K.T., Tarbell, T.D., Title, A.M., Torgerson, D.D., Golub, L., Bookbinder, J.A., Caldwell, D., Cheimets, P.N., Davis, W.N., Deluca, E.E., McMullen, R.A., Warren, H.P., Amato, D., Fisher, R., Maldonado, H., Parkinson, C.: 1999, The transition region and coronal explorer. *Solar Phys.* **187**, 229. DOI. ADS.

Hapgood, M.: 2017, *Space Weather*. DOI. ADS.

Harvey, K.: 2000, Coronal cavities. In: Murdin, P. (ed.) *Encyclopedia of Astronomy and Astrophysics* **2268**. DOI. ADS.

Harvey, J.W., Bolding, J., Clark, R., Hauth, D., Hill, F., Kroll, R., Luis, G., Mills, N., Purdy, T., Henney, C., Holland, D., Winter, J.: 2011, Full-disk Solar H-alpha images from GONG. In: *AAS/Solar Physics Div. Abs.* **42**, 17.45. ADS.

Hill, F.: 2018, The global oscillation network group facility—an example of research to operations in space weather. *Space Weather* **16**, 1488. DOI.

Hoeksema, J.T.: 1984, Structure and Evolution of the Large Scale Solar and Heliospheric Magnetic Fields. PhD thesis, Stanford University, California. ADS.

Howard, T.A., Harrison, R.A.: 2013, Stealth coronal mass ejections: a perspective. *Solar Phys.* **285**, 269. DOI. ADS.

Howard, R.A., Moses, J.D., Vourlidas, A., Newmark, J.S., Socker, D.G., Plunkett, S.P., Korendyke, C.M., Cook, J.W., Hurley, A., Davila, J.M., Thompson, W.T., St Cyr, O.C., Mentzell, E., Mehalick, K., Lemen, J.R., Wuelser, J.P., Duncan, D.W., Tarbell, T.D., Wolfson, C.J., Moore, A., Harrison, R.A., Waltham, N.R., Lang, J., Davis, C.J., Eyles, C.J., Mapson-Menard, H., Simnett, G.M., Halain, J.P., Defise, J.M., Mazy, E., Rochus, P., Mercier, R., Ravet, M.F., Delmotte, F., Auchere, F., Delaboudiniere, J.P., Bothmer, V., Deutsch, W., Wang, D., Rich, N., Cooper, S., Stephens, V., Maahs, G., Baugh, R., McMullin, D., Carter, T.: 2008, Sun Earth Connection Coronal and Heliospheric Investigation (SECCHI). *Space Sci. Rev.* **136**, 67. DOI. ADS.

Hudson, H.S.: 2000, Implosions in coronal transients. *Astrophys. J. Lett.* **531**, L75. DOI. ADS.

Hudson, H.S., Webb, D.F.: 1997, Soft X-ray signatures of coronal ejections. In: *Coronal Mass Ejections, Washington DC American Geophysical Union Geophysical Monograph Series* **99**, 27. DOI. ADS.

Inhester, B.: 2006, Stereoscopy basics for the STEREO mission. arXiv e-prints. astro. ADS.

Johri, A., Manoharan, P.K.: 2016, An intense flare-CME event in 2015: propagation and interaction effects between the Sun and Earth's orbit. *Solar Phys.* **291**, 1433. DOI. ADS.

Kaiser, M.L., Kucera, T.A., Davila, J.M., St. Cyr, O.C., Guhathakurta, M., Christian, E.: 2008, The STEREO mission: an introduction. *Space Sci. Rev.* **136**, 5. DOI. ADS.

Kerdraon, A., Delouis, J.-M.: 1997, The Nançay Radioheliograph. In: Trottet, G. (ed.) *Coronal Physics from Radio and Space Observations* **483**, 192. DOI. ADS.

Kienreich, I.W., Muhr, N., Veronig, A.M., Berghmans, D., De Groof, A., Temmer, M., Vršnak, B., Seaton, D.B.: 2013, Solar TErrestrial Relations Observatory-A (STEREO-A) and PRoject for On-Board Autonomy 2 (PROBA2) quadrature observations of reflections of three EUV waves from a coronal hole. *Solar Phys.* **286**, 201. DOI. ADS.

Kliem, B., Török, T.: 2006, Torus instability. *Phys. Rev. Lett.* **96**, 255002. DOI. ADS.

Koukras, A., Marqué, C., Downs, C., Dolla, L.: 2020, Analyzing the propagation of EUV waves and their connection with type II radio bursts by combining numerical simulations and multi-instrument observations. *Astron. Astrophys.* **644**, A90. DOI. ADS.

Koutchmy, S., Nikoghossian, A.G.: 2002, Coronal linear threads: W-L radiation of supra-thermal streams. *Astron. Astrophys.* **395**, 983. DOI. ADS.

Kruglanski, M., Devos, A., Calders, S., De Donder, E., Berghmans, D., Andries, J., Crosby, N., Dierckxsens, M., Glover, A.: 2017, Provision of space weather bulletins in support to ESA missions. In: *EGU General Assembly Conference Abstracts*, *EGU General Assembly Conference Abstracts*, 18071. ADS.

Kumar, P., Cho, K.-S.: 2014, Multiwavelength observation of a large-scale flux rope eruption above a kinked small filament. *Astron. Astrophys.* **572**, A83. DOI. ADS.

Laurenza, M., Cliver, E.W., Hewitt, J., Storini, M., Ling, A.G., Balch, C.C., Kaiser, M.L.: 2009, A technique for short-term warning of solar energetic particle events based on flare location, flare size, and evidence of particle escape. *Space Weather* **7**, S04008. DOI. ADS.

Lecacheux, A.: 2000, The Nançay decameter array: a useful step towards giant, new generation radio telescopes for long wavelength radio astronomy. *Geophys. Monogr. Ser.* **119**, 321. DOI. ADS.

Lemen, J.R., Title, A.M., Akin, D.J., Boerner, P.F., Chou, C., Drake, J.F., Duncan, D.W., Edwards, C.G., Friedlaender, F.M., Heyman, G.F., Hurlburt, N.E., Katz, N.L., Kushner, G.D., Levay, M., Lindgren, R.W., Mathur, D.P., McFeaters, E.L., Mitchell, S., Rehse, R.A., Schrijver, C.J., Springer, L.A., Stern, R.A., Tarbell, T.D., Wuelser, J.-P., Wolfson, C.J., Yanari, C., Bookbinder, J.A., Cheimets, P.N., Caldwell, D., Deluca, E.E., Gates, R., Golub, L., Park, S., Podgorski, W.A., Bush, R.I., Scherrer, P.H., Gummin, M.A., Smith, P., Auker, G., Jerram, P., Pool, P., Soufli, R., Windt, D.L., Beardsley, S., Clapp, M., Lang, J., Waltham, N.: 2012, The Atmospheric Imaging Assembly (AIA) on the Solar Dynamics Observatory (SDO). *Solar Phys.* **275**, 17. DOI. ADS.

Liu, J., Zhou, Z., Wang, Y., Liu, R., Wang, B., Liao, C., Shen, C., Zheng, H., Miao, B., Su, Z., Wang, S.: 2012, Slow magnetoacoustic waves observed above a quiet-sun region in a dark cavity. *Astrophys. J. Lett.* **758**, L26. DOI. ADS.

Luntama, J.-P., Glover, A., Kraft, S.: 2018, ESA SSA space weather activities and COSPAR-ILWS roadmap. In: *42nd COSPAR Scientific Assembly* **42**, PSW.5, ADS.

Lynch, B.J., Antiochos, S.K., MacNeice, P.J., Zurbuchen, T.H., Fisk, L.A.: 2004, Observable properties of the breakout model for coronal mass ejections. *Astrophys. J.* **617**, 589. DOI. ADS.

Maguire, C.A., Carley, E.P., Zucca, P., Vilmer, N., Gallagher, P.T.: 2021, LOFAR observations of a jet-driven piston shock in the low solar corona. *Astrophys. J.* **909**, 2. DOI. ADS.

Mampaey, B., Verbeeck, F., Stegen, K., Kraaikamp, E., Gissot, S., Auchère, F., Berghmans, D.: 2022, *SolO/EUI Data Release 5.0 2022–04*. DOI.

Mason, J.P., Chamberlin, P.C., Seaton, D., Burkepile, J., Colaninno, R., Dissauer, K., Eparvier, F.G., Fan, Y., Gibson, S., Jones, A.R., Kay, C., Kirk, M., Kohnert, R., Pesnell, W.D., Thompson, B.J., Veronig, A.M., West, M.J., Windt, D., Woods, T.N.: 2021, SunCET: the Sun coronal ejection tracker concept. *J. Space Weather Space Clim.* **11**, 20. DOI. ADS.

Mason, J.P., Seaton, D.B., Jones, A.R., Jin, M., Chamberlin, P.C., Sims, A., Woods, T.N.: 2022, Simultaneous high dynamic range algorithm, testing, and instrument simulation. *Astrophys. J.* **924**, 63. DOI. ADS.

Meyer, K.A., Mackay, D.H., Talpeanu, D.-C., Upton, L.A., West, M.J.: 2020, Investigation of the middle corona with SWAP and a data-driven non-potential coronal magnetic field model. *Solar Phys.* **295**, 101. DOI. ADS.

Mierla, M., Inhester, B., Antunes, A., Boursier, Y., Byrne, J.P., Colaninno, R., Davila, J., de Koning, C.A., Gallagher, P.T., Gissot, S., Howard, R.A., Howard, T.A., Kramar, M., Lamy, P., Liewer, P.C., Maloney, S., Marqué, C., McAteer, R.T.J., Moran, T., Rodriguez, L., Srivastava, N., St. Cyr, O.C., Stenborg, G., Temmer, M., Thernisien, A., Vourlidas, A., West, M.J., Wood, B.E., Zhukov, A.N.: 2010, On the 3-D reconstruction of coronal mass ejections using coronagraph data. *Ann. Geophys.* **28**, 203. DOI. ADS.

Mierla, M., Seaton, D.B., Berghmans, D., Chifu, I., De Groof, A., Inhester, B., Rodriguez, L., Stenborg, G., Zhukov, A.N.: 2013, Study of a prominence eruption using PROBA2/SWAP and STEREO/EUVI data. *Solar Phys.* **286**, 241. DOI. ADS.

Mierla, M., Janssens, J., D'Huys, E., Wauters, L., West, M.J., Seaton, D.B., Berghmans, D., Podladchikova, E.: 2020, Long-term evolution of the solar corona using PROBA2 data. *Solar Phys.* **295**, 66. DOI. ADS.

Morgan, H., Druckmüller, M.: 2014, Multi-scale Gaussian normalization for solar image processing. *Solar Phys.* **289**, 2945. DOI. ADS.

Morgan, H., Habbal, S.R.: 2007, Are solar maximum fan streamers a consequence of twisting sheet structures? *Astron. Astrophys.* **465**, L47. DOI. ADS.

Morosan, D.E., Kilpua, E.K.J., Carley, E.P., Monstein, C.: 2019, Variable emission mechanism of a Type IV radio burst. *Astron. Astrophys.* **623**, A63. DOI. ADS.

Müller, D., Marsden, R.G., St. Cyr, O.C., Gilbert, H.R.: 2013, Solar orbiter. Exploring the sun-heliosphere connection. *Solar Phys.* **285**, 25. DOI. ADS.

Müller, D., Nicula, B., Felix, S., Verstringe, F., Bourgoignie, B., Csillaghy, A., Berghmans, D., Jiggens, P., García-Ortiz, J.P., Ireland, J., Zahniy, S., Fleck, B.: 2017, JHelioviewer. Time-dependent 3D visualisation of solar and heliospheric data. *Astron. Astrophys.* **606**, A10. DOI. ADS.

O'Hara, J.P., Mierla, M., Podladchikova, O., D'Huys, E., West, M.J.: 2019, Exceptional extended field-of-view observations by PROBA2/SWAP on 2017 April 1 and 3. *Astrophys. J.* **883**, 59. DOI. ADS.

Olmedo, O., Zhang, J., Wechsler, H., Poland, A., Borne, K.: 2008, Automatic detection and tracking of coronal mass ejections in coronagraph time series. *Solar Phys.* **248**, 485. DOI. ADS.

Palmerio, E., Scolini, C., Barnes, D., Magdalenić, J., West, M.J., Zhukov, A.N., Rodriguez, L., Mierla, M., Good, S.W., Morosan, D.E., Kilpua, E.K.J., Pomoell, J., Poedts, S.: 2019, Multipoint study of successive coronal mass ejections driving moderate disturbances at 1 au. *Astrophys. J.* **878**, 37. DOI. ADS.

Panesar, N.K., Innes, D.E., Tiwari, S.K., Low, B.C.: 2013, A solar tornado triggered by flares? *Astron. Astrophys.* **549**, A105. DOI. ADS.

Parenti, S.: 2014, Solar prominences: observations. *Living Rev. Solar Phys.* **11**, 1. DOI. ADS.

Pasachoff, J.M., Rušin, V., Druckmüllerová, H., Saniga, M., Lu, M., Malamut, C., Seaton, D.B., Golub, L., Engell, A.J., Hill, S.W., Lucas, R.: 2011, Structure and dynamics of the 2010 July 11 eclipse white-light corona. *Astrophys. J.* **734**, 114. DOI. ADS.

Pasachoff, J.M., Rušin, V., Saniga, M., Babcock, B.A., Lu, M., Davis, A.B., Dantowitz, R., Gaintatzis, P., Seiradakis, J.H., Voulgaris, A., Seaton, D.B., Shiota, K.: 2015, Structure and dynamics of the 2012 November 13/14 eclipse white-light corona. *Astrophys. J.* **800**, 90. DOI. ADS.

Patel, R., Pant, V., Iyer, P., Banerjee, D., Mierla, M., West, M.J.: 2021, Automated detection of accelerating solar eruptions using parabolic hough transform. *Solar Phys.* **296**, 31. DOI. ADS.

Pesnell, W.D., Thompson, B.J., Chamberlin, P.C.: 2012, The Solar Dynamics Observatory (SDO). *Solar Phys.* **275**, 3. DOI. ADS.

Plowman, J.: 2016, A center-median filtering method for detection of temporal variation in coronal images. *J. Space Weather Space Clim.* **6**, A8. DOI. ADS.

Plowman, J., Kankelborg, C., Martens, P.: 2013, Fast differential emission measure inversion of solar coronal data. *Astrophys. J.* **771**, 2. DOI. ADS.

Pneuman, G.W., Kopp, R.A.: 1971, Gas-magnetic field interactions in the solar corona. *Solar Phys.* **18**, 258. DOI. ADS.

Priest, E.R., Forbes, T.G.: 2002, The magnetic nature of solar flares. *Astron. Astrophys. Rev.* **10**, 313. DOI. ADS.

Prusti, T., de Bruijne, J.H.J., Brown, A.G.A., Vallenari, A., Babusiaux, C., Bailer-Jones, C.A.L., Bastian, U., Biermann, M., Evans, D.W., Eyer, L., Jansen, F., Jordi, C., Klioner, S.A., Lammers, U., Lindegren, L., Luri, X., Mignard, F., Milligan, D.J., Panem, C., Poinsignon, V., Pourbaix, D., Randich, S., Sarri, G., Sartoretti, P., Siddiqui, H.I., Soubiran, C., Valette, V., van Leeuwen, F., Walton, N.A., Aerts, C., Arenou, F., Cropper, M., Drimmel, R., Høg, E., Katz, D., Lattanzi, M.G., O'Mullane, W., Grebel, E.K., Holland, A.D., Huc, C., Passot, X., Bramante, L., Cacciari, C., Castañeda, J., Chaoul, L., Cheek, N., De Angeli, F., Fabricius, C., Guerra, R., Hernández, J., Jean-Antoine-Piccolo, A., Masana, E., Messineo, R., Mowlavi, N., Nienartowicz, K., Ordóñez-Blanco, D., Panuzzo, P., Portell, J., Richards, P.J., Riello, M., Seabroke, G.M., Tanga, P., Thévenin, F., Torra, J., Els, S.G., Gracia-Abril, G., Comoretto, G., Garcia-Reinaldos, M., Lock, T., Mercier, E., Altmann, M., Andrae, R., Astraatmadja, T.L., Bellas-Velidis, I., Benson, K., Berthier, J., Blomme, R., Busso, G., Carry, B., Cellino, A., Clementini, G., Cowell, S., Creevey, O., Cuypers, J., Davidson, M., De Ridder, J., de Torres, A., Delchambre, L., Dell'Oro, A., Ducourant, C., Frémat, Y., García-Torres, M., Gosset, E., Halbwachs, J.-L., Hambly, N.C., Harrison, D.L., Hauser, M., Hestroffer, D., Hodgkin, S.T., Huckle, H.E., Hutton, A., Jasniewicz, G., Jordan, S., Kontizas, M., Korn, A.J., Lanzafame, A.C., Manteiga, M., Moitinho, A., Muinonen, K., Osinde, J., Pancino, E., Pauwels, T., Petit, J.-M., Recio-Blanco, A., Robin, A.C., Sarro, L.M., Siopis, C., Smith, M., Smith, K.W., Sozzetti, A., Thuillot, W., van Reeven, W., Viala, Y., Abbas, U., Abreu Aramburu, A., Accart, S., Aguado, J.J., Allan, P.M., Allasia, W., Altavilla, G., Álvarez, M.A., Alves, J., Anderson, R.I., Andrei, A.H., Anglada Varela, E., Antiche, E., Antoja, T., Antón, S., Arcay, B., Atzei, A., Ayache, L., Bach, N., Baker, S.G., Balaguer-Núñez, L., Barache, C., Barata, C., Barbier, A., Barblan, F., Baroni, M., Barrado y Navascués, D., Barros, M., Barstow, M.A., Becciani, U., Bellazzini, M., Bellei, G., Bello García, A., Belokurov, V., Bendjoya, P., Berihuete, A., Bianchi, L., Bienaymé, O., Billebaud, F., Blagorodnova, N., Blanco-Cuaresma, S., Boch, T., Bombrun, A., Borrachero, R., Bouquillon, S., Bourda, G., Bouy, H., Bragaglia, A., Breddels, M.A., Brouillet, N., Brüsemeister, T., Bucciarelli, B., Budnik, F., Burgess, P., Burgon, R., Burlacu, A., Busonero, D., Buzzi, R., Caffau, E., Cambras, J., Campbell, H., Cancelliere, R., Cantat-Gaudin, T., Carlucci, T., Carrasco, J.M., Castellani, M., Charlot, P., Charnas, J., Charvet, P., Chassat, F., Chiavassa, A., Clotet, M., Cocozza, G., Collins, R.S., Collins, P., Costigan, G., Crifo, F., Cross, N.J.G., Crosta, M., Crowley, C., Dafonte, C., Damerdji, Y., Dapergolas, A., David, P., David, M., De Cat, P., de Felice, F., de Laverny, P., De Luise, F., De March, R., de Martino, D., de Souza, R., Debosscher, J., del Pozo, E., Delbo, M., Delgado, A., Delgado, H.E., di Marco, F., Di Matteo, P., Diakite, S., Distefano, E., Dolding, C., Dos Anjos, S., Drazinos, P., Durán, J., Dzigan, Y., Ecale, E., Edvardsson, B., Enke, H., Erdmann, M., Escolar, D., Espina, M., Evans, N.W., Eynard Bontemps, G., Fabre, C., Fabrizio, M., Faigler, S., Falcão, A.J., Farràs Casas, M., Faye, F., Federici, L., Fedorets, G., Fernández-Hernández,

J., Fernique, P., Fienga, A., Figueras, F., Filippi, F., Findeisen, K., Fonti, A., Fouesneau, M., Fraile, E., Fraser, M., Fuchs, J., Furnell, R., Gai, M., Galleti, S., Galluccio, L., Garabato, D., García-Sedano, F., Garé, P., Garofalo, A., Garralda, N., Gavras, P., Gerssen, J., Geyer, R., Gilmore, G., Girona, S., Giuffrida, G., Gomes, M., González-Marcos, A., González-Núñez, J., González-Vidal, J.J., Granvik, M., Guerrier, A., Guillout, P., Guiraud, J., Gúrpide, A., Gutiérrez-Sánchez, R., Guy, L.P., Haigron, R., Hatzidimitriou, D., Haywood, M., Heiter, U., Helmi, A., Hobbs, D., Hofmann, W., Holl, B., Holland, G., Hunt, J.A.S., Hypki, A., Icardi, V., Irwin, M., Jevardat de Fombelle, G., Jofré, P., Jonker, P.G., Jorissen, A., Julbe, F., Karampelas, A., Kochoska, A., Kohley, R., Kolenberg, K., Kontizas, E., Koposov, S.E., Kordopatis, G., Koubsky, P., Kowalczyk, A., Krone-Martins, A., Kudryashova, M., Kull, I., Bachchan, R.K., Lacoste-Seris, F., Lanza, A.F., Lavigne, J.-B., Le Poncin-Lafitte, C., Lebreton, Y., Lebzelter, T., Leccia, S., Leclerc, N., Lecoeur-Taibi, I., Lemaitre, V., Lenhardt, H., Leroux, F., Liao, S., Licata, E., Lindstrøm, H.E.P., Lister, T.A., Livanou, E., Lobel, A., Löffler, W., López, M., Lopez-Lozano, A., Lorenz, D., Loureiro, T., MacDonald, I., Magalhães Fernandes, T., Managau, S., Mann, R.G., Mantelet, G., Marchal, O., Marchant, J.M., Marconi, M., Marie, J., Marinoni, S., Marrese, P.M., Marschalkó, G., Marshall, D.J., Martín-Fleitas, J.M., Martino, M., Mary, N., Matijevič, G., Mazeh, T., McMillan, P.J., Messina, S., Mestre, A., Michalik, D., Millar, N.R., Miranda, B.M.H., Molina, D., Molinaro, R., Molinaro, M., Molnár, L., Moniez, M., Montegriffo, P., Monteiro, D., Mor, R., Mora, A., Morbidelli, R., Morel, T., Morgenthaler, S., Morley, T., Morris, D., Mulone, A.F., Muraveva, T., Musella, I., Narbonne, J., Nelemans, G., Nicastro, L., Noval, L., Ordénovic, C., Ordieres-Meré, J., Osborne, P., Pagani, C., Pagano, I., Pailler, F., Palacin, H., Palaversa, L., Parsons, P., Paulsen, T., Pecoraro, M., Pedrosa, R., Pentikäinen, H., Pereira, J., Pichon, B., Piersimoni, A.M., Pineau, F.-X., Plachy, E., Plum, G., Poujoulet, E., Prša, A., Pulone, L., Ragaini, S., Rago, S., Rambaux, N., Ramos-Lerate, M., Ranalli, P., Rauw, G., Read, A., Regibo, S., Renk, F., Reylé, C., Ribeiro, R.A., Rimoldini, L., Ripepi, V., Riva, A., Rixon, G., Roelens, M., Romero-Gómez, M., Rowell, N., Royer, F., Rudolph, A., Ruiz-Dern, L., Sadowski, G., Sagristà Sellés, T., Sahlmann, J., Salgado, J., Salguero, E., Sarasso, M., Savietto, H., Schnorhk, A., Schultheis, M., Sciacca, E., Segol, M., Segovia, J.C., Segransan, D., Serpell, E., Shih, I.-C., Smareglia, R., Smart, R.L., Smith, C., Solano, E., Solitro, F., Sordo, R., Soria Nieto, S., Souchay, J., Spagna, A., Spoto, F., Stampa, U., Steele, I.A., Steidelmüller, H., Stephenson, C.A., Stoev, H., Suess, F.F., Süveges, M., Surdej, J., Szabados, L., Szegedi-Elek, E., Tapiador, D., Taris, F., Tauran, G., Taylor, M.B., Teixeira, R., Terrett, D., Tingley, B., Trager, S.C., Turon, C., Ulla, A., Utrilla, E., Valentini, G., van Elteren, A., Van Hemelryck, E., van Leeuwen, M., Varadi, M., Vecchiato, A., Veljanoski, J., Via, T., Vicente, D., Vogt, S., Voss, H., Votruba, V., Voutsinas, S., Walmsley, G., Weiler, M., Weingrill, K., Werner, D., Wevers, T., Whitehead, G., Wyrzykowski, Ł., Yoldas, A., Žerjal, M., Zucker, S., Zurbach, C., Zwitter, T., Alecu, A., Allen, M., Allende Prieto, C., Amorim, A., Anglada-Escudé, G., Arsenijevic, V., Azaz, S., Balm, P., Beck, M., Bernstein, H.-H., Bigot, L., Bijaoui, A., Blasco, C., Bonfigli, M., Bono, G., Boudreault, S., Bressan, A., Brown, S., Brunet, P.-M., Bunclark, P., Buonanno, R., Butkevich, A.G., Carret, C., Carrion, C., Chemin, L., Chéreau, F., Corcione, L., Darmigny, E., de Boer, K.S., de Teodoro, P., de Zeeuw, P.T., Delle Luche, C., Domingues, C.D., Dubath, P., Fodor, F., Frézouls, B., Fries, A., Fustes, D., Fyfe, D., Gallardo, E., Gallegos, J., Gardiol, D., Gebran, M., Gomboc, A., Gómez, A., Grux, E., Gueguen, A., Heyrovsky, A., Hoar, J., Iannicola, G., Isasi Parache, Y., Janotto, A.-M., Joliet, E., Jonckheere, A., Keil, R., Kim, D.-W., Klagyivik, P., Klar, J., Knude, J., Kochukhov, O., Kolka, I., Kos, J., Kutka, A., Lainey, V., LeBouquin, D., Liu, C., Loreggia, D., Makarov, V.V., Marseille, M.G., Martayan, C., Martinez-Rubi, O., Massart, B., Meynadier, F., Mignot, S., Munari, U., Nguyen, A.-T., Nordlander, T., Ocvirk, P., O'Flaherty, K.S., Olias Sanz, A., Ortiz, P., Osorio, J., Oszkiewicz, D., Ouzounis, A., Palmer, M., Park, P., Pasquato, E., Peltzer, C., Peralta, J., Péturaud, F., Pieniluoma, T., Pigozzi, E., Poels, J., Prat, G., Prod'homme, T., Raison, F., Rebordao, J.M., Risquez, D., Rocca-Volmerange, B., Rosen, S., Ruiz-Fuertes, M.I., Russo, F., Sembay, S., Serraller Vizcaino, I., Short, A., Siebert, A., Silva, H., Sinachopoulos, D., Slezak, E., Soffel, M., Sosnowska, D., Straižys, V., ter Linden, M., Terrell, D., Theil, S., Tiede, C., Troisi, L., Tsalmantza, P., Tur, D., Vaccari, M., Vachier, F., Valles, P., Van Hamme, W., Veltz, L., Virtanen, J., Wallut, J.-M., Wichmann, R., Wilkinson, M.I., Ziaeepour, H., Zschocke, S. (Gaia Collaboration): 2016, The Gaia mission. *Astron. Astrophys.* **595**, A1. DOI. ADS.

Rachmeler, L.A., Gibson, S.E., Dove, J.B., DeVore, C.R., Fan, Y.: 2013, Polarimetric properties of flux ropes and sheared arcades in coronal prominence cavities. *Solar Phys.* **288**, 617. DOI. ADS.

Rachmeler, L.A., Platten, S.J., Bethge, C., Seaton, D.B., Yeates, A.R.: 2014, Observations of a hybrid double-streamer/pseudostreamer in the solar corona. *Astrophys. J. Lett.* **787**, L3. DOI. ADS.

Raftery, C.L., Bloomfield, D.S., Gallagher, P.T., Seaton, D.B., Berghmans, D., De Groof, A.: 2013, Temperature response of the 171 Å passband of the SWAP imager on PROBA2, with a comparison to TRACE, SOHO, STEREO, and SDO. *Solar Phys.* **286**, 111. DOI. ADS.

Reid, H.A.S., Ratcliffe, H.: 2014, A review of solar Type III radio bursts. *Res. Astron. Astrophys.* **14**, 773. DOI.

Reva, A.A., Kirichenko, A.S., Ulyanov, A.S., Kuzin, S.V.: 2017, Observations of the coronal mass ejection with a complex acceleration profile. *Astrophys. J.* **851**, 108. DOI. ADS.

Robbrecht, E., Patsourakos, S., Vourlidas, A.: 2009, No trace left behind: STEREO observation of a coronal mass ejection without low coronal signatures. *Astrophys. J.* **701**, 283. DOI. ADS.

Rochus, P., Auchère, F., Berghmans, D., Harra, L., Schmutz, W., Schühle, U., Addison, P., Appourchaux, T., Aznar Cuadrado, R., Baker, D., Barbay, J., Bates, D., BenMoussa, A., Bergmann, M., Beurthe, C., Borgo, B., Bonte, K., Bouzit, M., Bradley, L., Büchel, V., Buchlin, E., Büchner, J., Cabé, F., Cadiergues, L., Chaigneau, M., Chares, B., Choque Cortez, C., Coker, P., Condamin, M., Coumar, S., Curdt, W., Cutler, J., Davies, D., Davison, G., Defise, J.-M., Del Zanna, G., Delmotte, F., Delouille, V., Dolla, L., Dumesnil, C., Dürig, F., Enge, R., François, S., Fourmond, J.-J., Gillis, J.-M., Giordanengo, B., Gissot, S., Green, L.M., Guerreiro, N., Guilbaud, A., Gyo, M., Haberreiter, M., Hafiz, A., Hailey, M., Halain, J.-P., Hansotte, J., Hecquet, C., Heerlein, K., Hellin, M.-L., Hemsley, S., Hermans, A., Hervier, V., Hochedez, J.-F., Houbrechts, Y., Ihsan, K., Jacques, L., Jérôme, A., Jones, J., Kahle, M., Kennedy, T., Klaproth, M., Kolleck, M., Koller, S., Kotsialos, E., Kraaikamp, E., Langer, C., Lawrenson, A., Le Clech', J.-C., Lenaerts, C., Liebecq, S., Linder, D., Long, D.M., Mampaey, B., Markiewicz-Innes, D., Marquet, B., Marsch, E., Matthews, S., Mazy, E., Mazzoli, A., Meining, S., Meltchakov, E., Mercier, R., Meyer, S., Monecke, M., Monfort, F., Morinaud, G., Moron, F., Mountney, L., Müller, R., Nicula, B., Parenti, S., Peter, H., Pfiffner, D., Philippon, A., Phillips, I., Plesseria, J.-Y., Pylyser, E., Rabecki, F., Ravet-Krill, M.-F., Rebellato, J., Renotte, E., Rodriguez, L., Roose, S., Rosin, J., Rossi, L., Roth, P., Rouesnel, F., Roulliay, M., Rousseau, A., Ruane, K., Scanlan, J., Schlatter, P., Seaton, D.B., Silliman, K., Smit, S., Smith, P.J., Solanki, S.K., Spescha, M., Spencer, A., Stegen, K., Stockman, Y., Szwec, N., Tamiatto, C., Tandy, J., Teriaca, L., Theobald, C., Tychon, I., van Driel-Gesztelyi, L., Verbeeck, C., Vial, J.-C., Werner, S., West, M.J., Westwood, D., Wiegelmann, T., Willis, G., Winter, B., Zerr, A., Zhang, X., Zhukov, A.N.: 2020, The solar orbiter EUI instrument: the extreme ultraviolet imager. *Astron. Astrophys.* **642**, A8. DOI. ADS.

Rodriguez, L., Zhukov, A.N., Cid, C., Cerrato, Y., Saiz, E., Cremades, H., Dasso, S., Menvielle, M., Aran, A., Mandrini, C., Poedts, S., Schmieder, B.: 2009, Three frontside full halo coronal mass ejections with a nontypical geomagnetic response. *Space Weather* **7**, S06003. DOI. ADS.

Santandrea, S., Gantois, K., Strauch, K., Teston, F., Tilmans, E., Baijot, C., Gerrits, D., De Groof, A., Schwehm, G., Zender, J.: 2013, PROBA2: mission and spacecraft overview. *Solar Phys.* **286**, 5. DOI. ADS.

Sarkar, R., Srivastava, N., Mierla, M., West, M.J., D'Huys, E.: 2019, Evolution of the coronal cavity from the quiescent to eruptive phase associated with coronal mass ejection. *Astrophys. J.* **875**, 101. DOI. ADS.

Savage, S.L., McKenzie, D.E., Reeves, K.K.: 2012, Re-interpretation of supra-arcade downflows in solar flares. *Astrophys. J. Lett.* **747**, L40. DOI. ADS.

Schou, J., Scherrer, P.H., Bush, R.I., Wachter, R., Couvidat, S., Rabello-Soares, M.C., Bogart, R.S., Hoeksema, J.T., Liu, Y., Duvall, T.L., Akin, D.J., Allard, B.A., Miles, J.W., Rairden, R., Shine, R.A., Tarbell, T.D., Title, A.M., Wolfson, C.J., Elmore, D.F., Norton, A.A., Tomczyk, S.: 2012, Design and ground calibration of the Helioseismic and Magnetic Imager (HMI) instrument on the Solar Dynamics Observatory (SDO). *Solar Phys.* **275**, 229. DOI. ADS.

Schrijver, C.J., De Rosa, M.L.: 2003, Photospheric and heliospheric magnetic fields. *Solar Phys.* **212**, 165. DOI. ADS.

Schrijver, C.J., McMullen, R.A.: 2000, A case for resonant scattering in the quiet solar corona in extreme-ultraviolet lines with high oscillator strengths. *Astrophys. J.* **531**, 1121. DOI. ADS.

Schrijver, C.J., Elmore, C., Kliem, B., Török, T., Title, A.M.: 2008, Observations and modeling of the early acceleration phase of erupting filaments involved in coronal mass ejections. *Astrophys. J.* **674**, 586. DOI. ADS.

Seaton, D.B., Mierla, M., Berghmans, D., Zhukov, A.N., Dolla, L.: 2011, SWAP-SECCHI observations of a mass-loading type solar eruption. *Astrophys. J. Lett.* **727**, L10. DOI. ADS.

Seaton, D.B., De Groof, A., Shearer, P., Berghmans, D., Nicula, B.: 2013a, SWAP observations of the long-term, large-scale evolution of the extreme-ultraviolet solar corona. *Astrophys. J.* **777**, 72. DOI. ADS.

Seaton, D.B., Berghmans, D., Nicula, B., Halain, J.-P., De Groof, A., Thibert, T., Bloomfield, D.S., Raftery, C.L., Gallagher, P.T., Auchère, F., Defise, J.-M., D'Huys, E., Lecat, J.-H., Mazy, E., Rochus, P., Rossi, L., Schühle, U., Slemzin, V., Yalim, M.S., Zender, J.: 2013b, The SWAP EUV imaging telescope Part I: instrument overview and pre-flight testing. *Solar Phys.* **286**, 43. DOI. ADS.

Seaton, D.B., Hughes, J.M., Tadikonda, S.K., Caspi, A., DeForest, C.E., Krimchansky, A., Hurlburt, N.E., Seguin, R., Slater, G.: 2021, The Sun's dynamic extended corona observed in extreme ultraviolet. *Nat. Astron.* **5**, 1029. DOI. ADS.

Seetha, S., Megala, S.: 2017, Aditya-L1 mission. *Curr. Sci.* **113**, 610. DOI. ADS.

Shen, C., Chen, B., Reeves, K.K., Yu, S., Polito, V., Xie, X.: 2022, The origin of underdense plasma downflows associated with magnetic reconnection in solar flares. *Nat. Astron.* **6**, 317. DOI. ADS.

Shestov, S.V., Zhukov, A.N., Inhester, B., Dolla, L., Mierla, M.: 2021, Expected performances of the PROBA-3/ASPIICS solar coronagraph: simulated data. *Astron. Astrophys.* **652**, A4. DOI. ADS.

Sieyra, M.V., Cécere, M., Cremades, H., Iglesias, F.A., Sahade, A., Mierla, M., Stenborg, G., Costa, A., West, M.J., D'Huys, E.: 2020, Analysis of large deflections of prominence-CME events during the rising phase of Solar Cycle 24. *Solar Phys.* **295**, 126. DOI. ADS.

Sterling, A.C., Moore, R.L., Falconer, D.A., Adams, M.: 2015, Small-scale filament eruptions as the driver of X-ray jets in solar coronal holes. *Nature* **523**, 437. DOI. ADS.

Swarup, G., Sarma, N.V.G., Joshi, M.N., Kapahi, V.K., Bagri, D.S., Damle, S.H., Ananthakrishnan, S., Balasubramanian, V., Bhave, S.S., Sinha, R.P.: 1971, Large steerable radio telescope at Ootacamund, India. *Nat. Phys. Sci.* **230**, 185. DOI. ADS.

Tavabi, E., Koutchmy, S., Bazin, C.: 2018, Analysis of a failed eclipse plasma ejection using EUV observations. *Solar Phys.* **293**, 42. DOI. ADS.

Temmer, M.: 2021, Space weather: the solar perspective. *Living Rev. Solar Phys.* **18**, 4. DOI. ADS.

Thernisien, A.F.R., Howard, R.A., Vourlidas, A.: 2006, Modeling of flux rope coronal mass ejections. *Astrophys. J.* **652**, 763. DOI. ADS.

Thernisien, A., Vourlidas, A., Howard, R.A.: 2009, Forward modeling of coronal mass ejections using STEREO/SECCHI data. *Solar Phys.* **256**, 111. DOI. ADS.

Thompson, B.J., Myers, D.C.: 2009, A catalog of coronal "EIT wave" transients. *Astrophys. J. Suppl.* **183**, 225. DOI. ADS.

Thompson, B.J., Plunkett, S.P., Gurman, J.B., Newmark, J.S., St. Cyr, O.C., Michels, D.J.: 1998, SOHO/EIT observations of an Earth-directed coronal mass ejection on May 12, 1997. *Geophys. Res. Lett.* **25**, 2465. DOI. ADS.

Titov, D.V., Svedhem, H., McCoy, D., Lebreton, J.-P., Barabash, S., Bertaux, J.-L., Drossart, P., Formisano, V., Haeusler, B., Korablev, O.I., Markiewicz, W., Neveance, D., Petzold, M., Piccioni, G., Zhang, T.L., Taylor, F.W., Lellouch, E., Koschny, D., Witasse, O., Warhaut, M., Acomazzo, A., Rodrigues-Cannabal, J., Fabrega, J., Schirmann, T., Clochet, A., Coradini, M.: 2006, Venus Express: scientific goals, instrumentation, and scenario of the mission. *Cosm. Res.* **44**, 334. DOI. ADS.

Titov, V.S., Mikic, Z., Török, T., Linker, J.A., Panasenco, O.: 2012, 2010 August 1 – 2 sympathetic eruptions. I. Magnetic topology of the source-surface background field. *Astrophys. J.* **759**, 70. DOI. ADS.

Tomczyk, S., Card, G.L., Darnell, T., Elmore, D.F., Lull, R., Nelson, P.G., Streander, K.V., Burkepile, J., Casini, R., Judge, P.G.: 2008, An instrument to measure coronal emission line polarization. *Solar Phys.* **247**, 411. DOI. ADS.

Tun, S.D., Vourlidas, A.: 2013, Derivation of the magnetic field in a coronal mass ejection core via multi-frequency radio imaging. *Astrophys. J.* **766**, 130. DOI. ADS.

van Haarlem, M.P., Wise, M.W., Gunst, A.W., Heald, G., McKean, J.P., Hessels, J.W.T., de Bruyn, A.G., Nijboer, R., Swinbank, J., Fallows, R., et al.: 2013, LOFAR: the LOw-Frequency ARray. *Astron. Astrophys.* **556**, A2. DOI. ADS.

Wang, Y.-M., Sheeley, J.N.R., Rich, N.B.: 2007, Coronal pseudostreamers. *Astrophys. J.* **658**, 1340. DOI. ADS.

Webb, D.F., Howard, T.A.: 2012, Coronal mass ejections: observations. *Living Rev. Solar Phys.* **9**, 3. DOI. ADS.

West, M.J., Seaton, D.B.: 2015, SWAP observations of post-flare giant arches in the long-duration 14 October 2014 solar eruption. *Astrophys. J. Lett.* **801**, L6. DOI. ADS.

West, M.J., Zhukov, A.N., Dolla, L., Rodriguez, L.: 2011, Coronal seismology using EIT waves: estimation of the coronal magnetic field strength in the quiet sun. *Astrophys. J.* **730**, 122. DOI. ADS.

West, M.J., Kintziger, C., Haberreiter, M., Gyo, M., Berghmans, D., Gissot, S., Büchel, V., Golub, L., Shestov, S., Davies, J.A.: 2020, LUCI onboard Lagrange, the next generation of EUV space weather monitoring. *J. Space Weather Space Clim.* **10**, 49. DOI. ADS.

Witasse, O., Sánchez-Cano, B., Mays, M.L., Kajdič, P., Opgenoorth, H., Elliott, H.A., Richardson, I.G., Zouganelis, I., Zender, J., Wimmer-Schweingruber, R.F., Turc, L., Taylor, M.G.G.T., Roussos, E., Rouillard, A., Richter, I., Richardson, J.D., Ramstad, R., Provan, G., Posner, A., Plaut, J.J., Odstrcil, D., Nilsson, H., Niemenen, P., Milan, S.E., Mandt, K., Lohf, H., Lester, M., Lebreton, J.-P., Kuulkers, E., Krupp, N., Koenders, C., James, M.K., Intzekara, D., Holmstrom, M., Hassler, D.M., Hall, B.E.S., Guo, J., Goldstein, R., Goetz, C., Glassmeier, K.H., Génot, V., Evans, H., Espley, J., Edberg, N.J.T., Dougherty, M., Cowley, S.W.H., Burch, J., Behar, E., Barabash, S., Andrews, D.J., Altobelli, N.: 2017, Interplanetary coronal mass ejection observed at STEREO-A, Mars, comet 67P/Churyumov-Gerasimenko, Saturn, and New Horizons en route to Pluto: comparison of its Forbush decreases at 1.4, 3.1, and 9.9 AU. *J. Geophys. Res.* **122**, 7865. DOI. ADS.

Wuelser, J.-P., Lemen, J.R., Tarbell, T.D., Wolfson, C.J., Cannon, J.C., Carpenter, B.A., Duncan, D.W., Gradwohl, G.S., Meyer, S.B., Moore, A.S., Navarro, R.L., Pearson, J.D., Rossi, G.R., Springer, L.A., Howard, R.A., Moses, J.D., Newmark, J.S., Delaboudiniere, J.-P., Artzner, G.E., Auchere, F., Bougnet,

M., Bouyries, P., Bridou, F., Clotaire, J.-Y., Colas, G., Delmotte, F., Jerome, A., Lamare, M., Mercier, R., Mullot, M., Ravet, M.-F., Song, X., Bothmer, V., Deutsch, W.: 2004, EUVI: the STEREO-SECCHI extreme ultraviolet imager. In: Fineschi, S., Gummin, M.A. (eds.) *Telescopes and Instrumentation for Solar Astrophysics*, *Society of Photo-Optical Instrumentation Engineers (SPIE) Conference Series* **5171**, 111. DOI. ADS.

Wyper, P.F., Antiochos, S.K., DeVore, C.R., Lynch, B.J., Karpen, J.T., Kumar, P.: 2021, A model for the coupled eruption of a pseudostreamer and helmet streamer. *Astrophys. J.* **909**, 54. DOI. ADS.

Yashiro, S., Gopalswamy, N., Michalek, G., St. Cyr, O.C., Plunkett, S.P., Rich, N.B., Howard, R.A.: 2004, A catalog of white light coronal mass ejections observed by the SOHO spacecraft. *J. Geophys. Res.* **109**, A07105. DOI. ADS.

Yeates, A.R., Mackay, D.H., van Ballegooijen, A.A.: 2008, Modelling the global solar corona II: coronal evolution and filament chirality comparison. *Solar Phys.* **247**, 103. DOI. ADS.

Yeates, A.R., Amari, T., Contopoulos, I., Feng, X., Mackay, D.H., Mikić, Z., Wiegelmann, T., Hutton, J., Lowder, C.A., Morgan, H., Petrie, G., Rachmeler, L.A., Upton, L.A., Canou, A., Chopin, P., Downs, C., Druckmüller, M., Linker, J.A., Seaton, D.B., Török, T.: 2018, Global non-potential magnetic models of the solar corona during the March 2015 eclipse. *Space Sci. Rev.* **214**, 99. DOI. ADS.

Young, C.A., Gallagher, P.T.: 2008, Multiscale edge detection in the corona. *Solar Phys.* **248**, 457. DOI. ADS.

Zhang, J., Dere, K.P.: 2006, A statistical study of main and residual accelerations of coronal mass ejections. *Astrophys. J.* **649**, 1100. DOI. ADS.

Zhang, J., Temmer, M., Gopalswamy, N., Malandraki, O., Nitta, N.V., Patsourakos, S., Shen, F., Vršnak, B., Wang, Y., Webb, D., Desai, M.I., Dissauer, K., Dresing, N., Dumbović, M., Feng, X., Heinemann, S.G., Laurenza, M., Lugaz, N., Zhuang, B.: 2021, Earth-affecting solar transients: a review of progresses in Solar Cycle 24. *Prog. Earth Planet. Sci.* **8**, 56. DOI. ADS.

Zhukov, A.N., Auchère, F.: 2004, On the nature of EIT waves, EUV dimmings and their link to CMEs. *Astron. Astrophys.* **427**, 705. DOI. ADS.